CrossMark

J͞M PAPERS

Linear stability analysis of two fluid columns of different densities and viscosities in a gravity field

Aditya Heru Prathama[1],† **and Carlos Pantano**[1]

[1]Department of Aerospace and Mechanical Engineering, University of Southern California, Los Angeles, CA 90089, USA

The linear stability of a vertical interface separating two miscible fluid columns of different densities and viscosities under the influence of gravity is investigated. This flow possesses a time-dependent reference state (each column accelerates at different rates owing to their different densities) and the interface thickness grows as the square root of time (by diffusion). Numerical integration of the linear initial-value problem is carried out and discussed in detail as a function of vertical and spanwise wavenumbers and the flow parameters. Adjoint-based optimization is performed in order to determine initial conditions that lead to maximum growth of disturbances in finite time. Results indicate that the rate of growth of the perturbation energy at small wavenumbers (less affected by viscosity initially) is dominated by two-dimensional modes (no spanwise variation). Substantial transient growth is observed at higher wave modes initially, followed by asymptotic decay of the perturbations at large time. Sensitivity of perturbation growth with respect to initial time, density and viscosity ratios is investigated. This work is complementary to previous inviscid analysis of this configuration, which showed that the interface was unconditionally unstable at all wave modes, even in the presence of surface tension, and that instability grew as the exponential of time squared.

Key words: baroclinic flows, shear layers

1. Introduction

Rayleigh–Taylor instability (RTI) and Kelvin–Helmholtz instability (KHI) arise in natural phenomena as well as in technological applications, such as inertial confinement fusion, geophysics, astrophysics, compressible turbulent flows and combustion (Sharp 1984; Olson *et al.* 2011; Gat *et al.* 2017), to name a few. Canonical RTI is experienced by an

† Email address for correspondence: prathama@usc.edu

920 A26-1

interface between two quiescent fluids where the heavier fluid is on top of the lighter one, while KHI takes place when there is shear across the interface of two fluids with different velocities and densities (Rayleigh 1883; Taylor 1950; Chandrasekhar 1981). In general, classical temporal stability theory has been focusing on quasi-parallel or parallel shear flows, either bounded (boundary layers, Poiseuille and Couette flows) or unbounded flows (jets, wakes and mixing layers), as well as flows in porous media (Truzzolillo & Cipelletti 2018). In atmospheric flows, the linear stability of a vertical interface between two fluids with different densities has been investigated in the case of shallow convection with or without wind shear (Bretherton 1987; Mellado 2017; Kirshbaum & Straub 2019). In these analyses, the domain is bounded in the vertical dimension, using homogeneous boundary conditions, and the base flow is assumed to be stationary. The linear stability analysis (LSA) then leads to time-independent linear differential equations for the flow perturbations which can be solved as a superposition of Fourier modes (Drazin & Reid 2004). Long-time instability is subsequently determined by the existence of the least stable eigenmode, with exponential growth rate indicated by the corresponding eigenvalue. However, it is well recognized that this approach fails to take into account the short-term dynamics between the mean flow and perturbation. For instance, plane Couette flow, which is linearly stable based on eigenvalue analysis alone, experiences large transient algebraic growth prior to asymptotic decay. This is attributed to the fact that the underlying linear operators are not self-adjoint (Reddy, Schmid & Henningson 1993; Trefethen *et al.* 1993). Their eigenfunctions are not mutually orthogonal and any initial perturbation constructed from an eigenfunction expansion may grow substantially (Gustavsson 1991; Butler & Farrell 1992; Reddy & Henningson 1993). In addition, modal analysis assumes that the base flow is steady or quasi-steady, commonly known as the quasi-steady-state approximation (QSSA), where the base flow is assumed to change at a lower rate than the perturbations. However, this yields erroneous results when analysing flows with time-dependent base states that evolve at time scales comparable to those of the perturbations. These problems can be analysed formally (if not really practically) using the initial-value problem (IVP) method (see the review of Schmid (2007)). Tan & Homsy (1986) carried out the LSA of an interface between two miscible fluids with different viscosities in porous media, utilizing both QSSA and IVP methods. They showed that the QSSA agrees poorly with results from the IVP at early times because the former ignores the rate of change of base state, which can be comparable to that of the fluctuations. Comparison between the growth of random noise and the eigenfunction from QSSA as initial conditions indicates that the latter case is less stable though. Ben, Demekhin & Chang (2002) employed the spectral method to investigate small-amplitude miscible fingering at inception, using a self-similar diffusive front as the base state. They argued that the QSSA is not valid at times where the fingers' amplitudes are much smaller than their wavelengths and their growth rate is small compared to the unsteady diffusive spreading rate of the base state. In general, it is known that the growth rate of disturbances is sensitive to the given initial condition (Tan & Homsy 1986) in the IVP formulation, and therefore it is not unique. Hence, it becomes of interest to determine the most amplified initial condition, usually up to a finite time horizon. Physically, this optimal growth arises from effective energy transfer from the mean flow to the non-mutually orthogonal modes (Farrell 1988). Several techniques such as eigenfunction expansion (Butler & Farrell 1992), expansion in periodic functions (Criminale, Jackson & Joslin 2003), singular value decomposition (Rapaka *et al.* 2008) and adjoint equations have been employed to determine linear optimal disturbances. The latter approach is used in this paper; see the review by Luchini & Bottaro (2014) for a detailed description of this method.

920 A26-2

In geophysical flows, Farrell & Moore (1992) used the adjoint of the quasi-geostrophic dynamic equations and performed the so-called direct-adjoint looping technique (Kaminski, Caulfield & Taylor 2014), an application of the power method. Corbett & Bottaro (2001) analysed the cross-flow instability in swept boundary layers, and found that the optimal disturbances take the form of nearly streamwise vortices at inception and develop into streaks. A similar study of Hiemenz flow with non-parallel base state at the leading edge of swept wings was also carried out to determine both optimal perturbations and optimal control (Guégan, Schmid & Huerre 2006). Later, Doumenc *et al.* (2010) and Daniel, Tilton & Riaz (2013) investigated the transient growth of perturbations in Rayleigh–Bénard–Marangoni convection and density-driven fingering, respectively. More recently, Arratia, Caulfield & Chomaz (2013) and Kaminski *et al.* (2014) studied the transient linear growth in homogeneous and parallel stratified shear layers, respectively. They found that at small enough Richardson number, the transient optimal perturbations are three-dimensional oblique waves due to Orr and lift-up mechanisms for small and large wavenumbers, respectively; the two-dimensional KHI is the dominant mechanism at large times. At large Richardson number, however, the modal instability is suppressed, and instead the growth of internal waves outside the vorticity layer is responsible for short-time amplification. These works were subsequently extended to a variable-density mixing layer experiencing the primary KHI (Lopez-Zazueta, Fontane & Joly 2016). Finally, more studies have been focusing on transient growth in porous media flows (Hota, Pramanik & Mishra 2015).

In the current study, a baroclinically generated shear layer formed between two vertically oriented columns with different densities and viscosities is considered. The columns are subject to an external gravitational acceleration field, resulting in initially perpendicular pressure and density gradients. While one is tempted to think of the flow as an RTI configuration, the situation resembles more a KHI flow of variable density where the velocities of the columns grow linearly in time. This canonical configuration has been recently investigated by Gat *et al.* (2016, 2017) using direct numerical simulation (DNS). Prathama & Pantano (2017) carried out the LSA of this configuration in the inviscid limit, with the presence of surface tension. The analysis is developed in the framework of an IVP (Richtmyer 1960), since the problem does not admit harmonic modal analysis. The analytic solution of the inviscid case indicates that the flow is unconditionally unstable at all wave modes, owing to the constantly accelerating columns that provide an unlimited source of kinetic energy. The growth of the solution is determined to be quadratic in time exponential. In this paper, we discuss the LSA of this configuration for miscible fluids with viscosity and diffusion and compare it with the inviscid limit results determined previously. In this variable-density flow, the velocity vector field is not divergence-free when there is diffusion of species (Gat *et al.* 2017; Lu & Pantano 2020). This precludes a conventional formulation of the problem in terms of the perturbation stream function.

The flow configuration and governing equations are described in §2, followed by the LSA in §3. Specifically, the base state is discussed in §3.1 and the IVP approach is elaborated in §3.2. Furthermore, adjoint optimization is carried out in order to determine the initial perturbation that yields maximum growth of disturbance energy at later times. Different choices of the objective functions are explored to clarify their impact on the conclusions. In §4, the results are presented and the sensitivities of perturbation growth with respect to initial time, density and viscosity ratios are discussed. Finally, results from a DNS study of Gat *et al.* (2017) are compared against those of LSA in §5, while concluding remarks are made in §6.
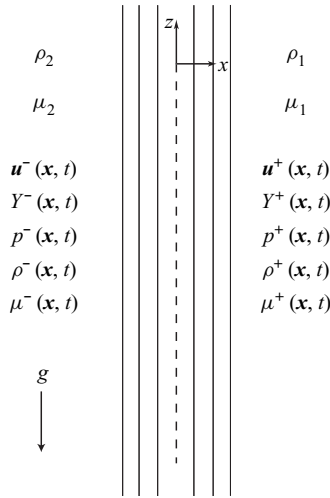
Figure 1. Planar sketch of flow configuration in Cartesian coordinates (y is perpendicular to the page).

2. Problem formulation

We consider the linear stability of a vertical interface separating two fluid columns of different densities and viscosities under the influence of gravity. Figure 1 illustrates the flow configuration, where a constant gravitational acceleration field g is acting downwards ($-\hat{z}$ direction), and the unperturbed interface is initially located along the z axis at $x = 0$. The density and viscosity of the right and left fluid columns are ρ_1, μ_1 and ρ_2, μ_2, respectively. The following constant parameters are introduced:

$$R \equiv \frac{\rho_1}{\rho_2}, \quad \bar{\rho} \equiv \frac{\rho_1 + \rho_2}{2}, \quad M \equiv \frac{\mu_1}{\mu_2}, \quad \bar{\mu} \equiv \frac{\mu_1 + \mu_2}{2}, \tag{2.1a–d}$$

where R is the density ratio of high- to low-density fluid and $\bar{\rho}$ is the average density; M and $\bar{\mu}$ are the dynamic viscosity ratio and the average viscosity, respectively.

The equations for conservation of linear momentum, species concentration and mass are given by

$$\rho \left(\frac{\partial \boldsymbol{u}}{\partial t} + \boldsymbol{u} \cdot \nabla \boldsymbol{u} \right) = -\nabla \tilde{p} - (\rho - \bar{\rho}) g \hat{z} + \nabla \cdot \left[\mu \left(\nabla \boldsymbol{u} + \nabla \boldsymbol{u}^T \right) \right], \tag{2.2}$$

$$\rho \left(\frac{\partial Y}{\partial t} + \boldsymbol{u} \cdot \nabla Y \right) = \nabla \cdot (\rho \, D \nabla Y), \tag{2.3}$$

$$\frac{\partial \rho}{\partial t} + \nabla \cdot (\rho \boldsymbol{u}) = 0, \tag{2.4}$$

where ρ is the density of the mixture, $\boldsymbol{u} = (u, v, w)$ is the velocity vector, $\tilde{p} = p - \frac{2}{3}\mu(\nabla \cdot \boldsymbol{u})$ is the modified pressure, μ is the dynamic viscosity of the mixture, Y is the heavy fluid mass fraction and D is the binary species diffusivity. For a binary mixture in the zero-Mach-number limit (Sandoval 1995; Gat *et al.* 2017), the density is related to the local mass fraction according to

$$\frac{1}{\rho(\boldsymbol{x}, t)} = \left(\frac{1}{\rho_1} - \frac{1}{\rho_2} \right) Y(\boldsymbol{x}, t) + \frac{1}{\rho_2}, \tag{2.5a}$$

and the dynamic viscosity is assumed to vary linearly with the local mass fraction according to

$$\mu(\boldsymbol{x}, t) = (\mu_1 - \mu_2) Y(\boldsymbol{x}, t) + \mu_2. \tag{2.5b}$$

Combining (2.3)–(2.4), while using (2.5a), one obtains the mass constraint equation (Lu & Pantano 2020), given by

$$\nabla \cdot \boldsymbol{u} = -\nabla \cdot \left(\frac{D}{\rho} \nabla \rho \right). \tag{2.6}$$

Now, we introduce the following non-dimensionalization:

$$x^* = \frac{x}{L}, \quad \tau^* = \frac{t}{T}, \quad \boldsymbol{u}^* = \frac{\boldsymbol{u}}{U}, \quad \tilde{p}^* = \frac{\tilde{p}}{\bar{\rho} U^2}, \quad \rho^* = \frac{\rho}{\bar{\rho}}, \quad \mu^* = \frac{\mu}{\bar{\mu}}, \tag{2.7a}$$

where the length, time and velocity scales of the mixing region are defined as

$$L = \left(\frac{\bar{\nu}^2}{g} \right)^{1/3}, \quad T = \left(\frac{\bar{\nu}}{g^2} \right)^{1/3}, \quad U = \frac{L}{T} = (\bar{\nu} g)^{1/3}, \tag{2.7b}$$

with $\bar{\nu} = \bar{\mu}/\bar{\rho}$ the average kinematic viscosity. The Reynolds number is unity with these scalings; another parameter of relevance is the dimensionless time τ, which is elaborated in § 3. The dimensionless governing equations become (dropping the asterisk and tilde notations)

$$\frac{\partial \boldsymbol{u}}{\partial \tau} + \boldsymbol{u} \cdot \nabla \boldsymbol{u} = -\frac{\nabla p}{\rho} - \left(1 - \frac{1}{\rho} \right) \hat{\boldsymbol{z}} + \frac{\nabla \cdot \left[\mu \left(\nabla \boldsymbol{u} + \nabla \boldsymbol{u}^T \right) \right]}{\rho}, \tag{2.8}$$

$$\frac{\partial Y}{\partial \tau} + \boldsymbol{u} \cdot \nabla Y = \frac{\nabla \cdot (\mu \nabla Y)}{Sc \, \rho}, \tag{2.9}$$

$$\nabla \cdot \boldsymbol{u} = \frac{1}{Sc} \nabla \cdot \left(\mu \nabla \frac{1}{\rho} \right), \tag{2.10}$$

where $Sc = (\mu/\rho)/D$ is the Schmidt number, i.e. the ratio of the viscous to the species diffusivity. Furthermore, (2.5a)–(2.5b) give the non-dimensional density and viscosity, according to

$$\frac{1}{\rho} = \frac{R+1}{2R} [R - (R-1)Y] \tag{2.11a}$$

and

$$\mu = \frac{2}{M+1} [1 + (M-1)Y], \tag{2.11b}$$

respectively.

3. Flow analysis for small perturbations

We introduce the following expansion for all flow fields in (2.8)–(2.10):

$$\boldsymbol{\Psi}(\boldsymbol{x}, \tau) = \boldsymbol{\Psi}_0(\boldsymbol{x}, \tau) + \epsilon \, \boldsymbol{\Psi}_1(\boldsymbol{x}, \tau) + O(\epsilon^2), \tag{3.1}$$

where $\boldsymbol{\Psi} = [u, v, w, Y, p]$ and ϵ is assumed to be very small. The subscripts 0 and 1 denote the base flow and the first-order perturbation fields, respectively. The latter are the main subject of this paper.

3.1. *Base flow*

The base state for this configuration is a function of x and τ only. There are no characteristic length and time scales in the flow, as can be seen from the scalings in (2.7b), which implies that the base flow is invariant under the stretching transformation $x \rightarrow ax$, $\tau \rightarrow a^2\tau$. This lowers the number of independent parameters from two to one, reducing the partial differential equations into ordinary ones (Ben *et al.* 2002). Therefore, it is expected that the base state will not depend on x and τ separately, since there are insufficient dimensional parameters in this problem (see the discussion on unsteady unidirectional flow in § 4.3 of Batchelor (1967)). Therefore, the base flow admits a self-similar solution, with the self-similar variable η defined as

$$\eta \equiv \frac{x}{\sqrt{2K\tau}}, \quad \text{where } K \equiv \frac{R+1}{RSc}. \tag{3.2}$$

Note that the self-similar solutions apply outside the singular instant corresponding to $\tau = 0$. This behaviour is typical in problems with similarity solution, e.g. Blasius boundary layer and unsteady unidirectional flow in unbounded domain (Batchelor 1967). Introducing the self-similar variable into the governing equations, where subscript '0' denotes the base flow fields, and using the auxiliary functions U_0, V_0, W_0, Y_0 and P_0, according to

$$u_0(x, \tau) = -\frac{(R-1)}{2}\sqrt{\frac{K}{2\tau}}\, U_0(\eta), \tag{3.3}$$

$$v_0(x, \tau) = V_0(\eta), \tag{3.4}$$

$$w_0(x, \tau) = \tau\, W_0(\eta), \tag{3.5}$$

$$Y_0(x, \tau) = Y_0(\eta), \tag{3.6}$$

$$p_0(x, \tau) = -\frac{(R-1)(2Sc-1)}{4Sc\,\tau}\, P_0(\eta), \tag{3.7}$$

one obtains the following system of equations:

$$U_0 = \mu_0 Y_0', \tag{3.8}$$

$$Z_0(\mu_0 V_0')' + \frac{1}{Sc}\left[(R-1)\mu_0 Y_0' + 2\eta\right] V_0' = 0, \tag{3.9}$$

$$Z_0(\mu_0 W_0')' + \frac{1}{Sc}\left[(R-1)\mu_0 Y_0' + 2\eta\right] W_0' - \frac{4}{Sc}(W_0 + 1) + 2KZ_0 = 0, \tag{3.10}$$

$$Z_0(\mu_0 Y_0')' + [(R-1)\mu_0 Y_0' + 2\eta]Y_0' = 0, \tag{3.11}$$

$$P_0 = \mu_0(\mu_0 Y_0'' + \beta Y_0'^2), \tag{3.12}$$

with primes denoting derivatives with respect to η, and

$$\mu_0(\eta) \equiv 1 + \beta\left(Y_0(\eta) - \frac{1}{2}\right), \quad Z_0(\eta) \equiv R - (R-1)Y_0(\eta), \quad \beta \equiv 2\left(\frac{M-1}{M+1}\right). \tag{3.13a–c}$$

The boundary conditions for the scalar are $Y_0(\eta \rightarrow \infty) \rightarrow 1$ and $Y_0(\eta \rightarrow -\infty) \rightarrow 0$ at the regions of heavier and lighter fluids, respectively. All other quantities, except w_0, approach zero far from the interface. The spatial discretization is carried out using a spectral collocation method based on Chebyshev polynomials, which is realized using
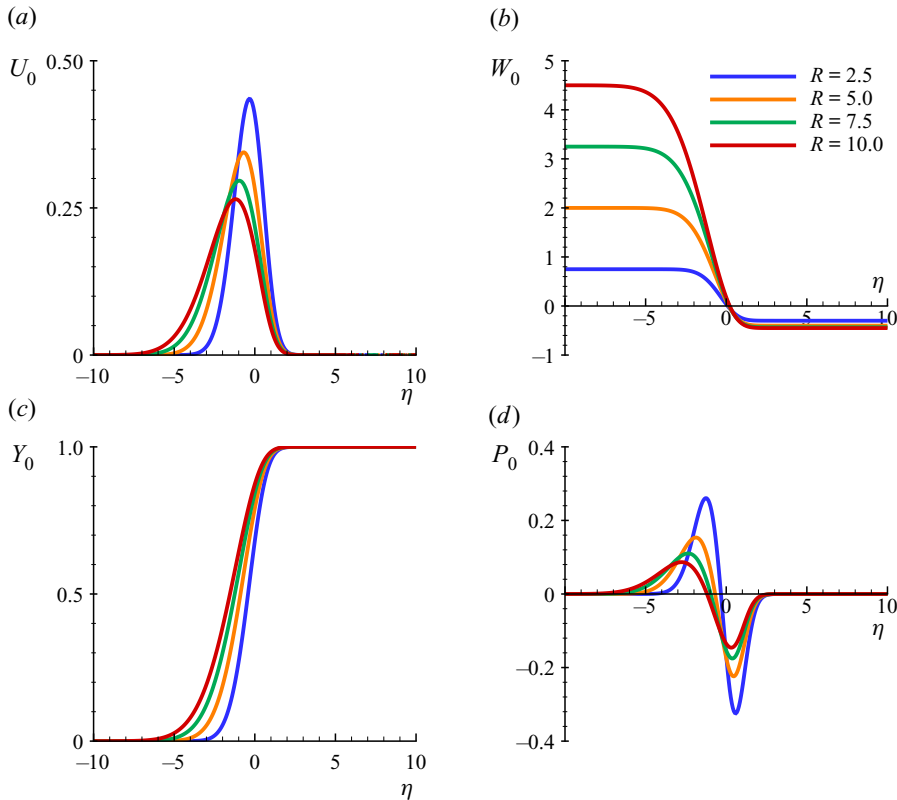
920 A26-6

Figure 2. Base flow fields as a function of density ratio R at uniform viscosity $M = 1$.

the open-source package *Chebfun* (Driscoll, Hale & Trefethen 2014; Aurentz & Trefethen 2017). The nonlinear boundary value problems are then solved with Newton's method. Figure 2 shows the solutions of the base flow fields as a function of η for several values of density ratio R and uniform viscosity ($M = 1$). One can observe the asymmetry of the $Y_0(\eta)$ profiles, where the heavier fluid is encroaching more into the lighter fluid region as R increases. However, the horizontal velocity U_0 and pressure P_0 are more concentrated with higher peaks for lower R and more spread with lower peaks at higher R. Finally, the vertical velocity W_0 profiles show larger relative velocities between the two columns as R increases. Note that both fluids move in the direction of the external uniform acceleration field in an inertial reference frame, while here one adopts a frame moving downwards with the average velocity of the columns (see Gat *et al.* (2017) for details). Figure 3 shows the effect of varying the viscosity ratio M, while keeping the density ratio constant at $R = 5$. Comparison with the previous case indicates that the influence of non-uniform viscosity plays a weaker role in the base flow behaviour than that of the density ratio.

3.2. *Initial-value problem*

We adopt the following Fourier decomposition of the first-order perturbation fields along the homogeneous directions:

$$(u_1, v_1, w_1, Y_1, p_1) = [\hat{U}(\eta, \tau), \hat{V}(\eta, \tau), \hat{W}(\eta, \tau), \hat{Y}(\eta, \tau), \hat{P}(\eta, \tau)]$$
$$\times \exp(\mathrm{i}(ky + mz)) + \text{c.c.}, \tag{3.14}$$

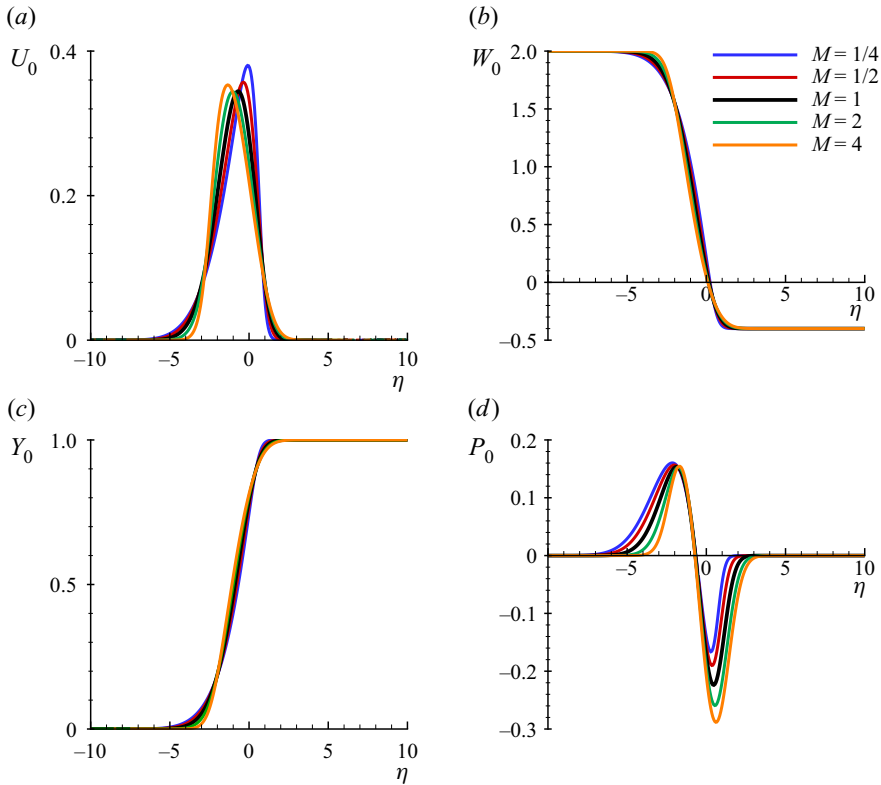(*a*)

(*b*)

(*c*)

(*d*)

Figure 3. Base flow fields as a function of viscosity ratio M at $R = 5$.

which transforms the problem into an IVP of the form

$$\frac{\partial \hat{X}}{\partial \tau} = L\left(Sc, R, M, k, m, \tau\right) \hat{X}, \tag{3.15}$$

where $\hat{X} = (\hat{U}, \hat{V}, \hat{W}, \hat{Y})$. The detailed expressions of (3.15) and the operator L are documented in Appendix A. Homogeneous boundary conditions are imposed at far fields, $\eta \to \pm\infty$, as we expect the perturbation fields to be localized in the vicinity of the mixing region. In this study, the equations are written in the frame of the self-similar coordinate, η. From this point of view, the base profiles look stationary, and time dependence is transferred to the governing equation, (3.15), as an explicit dependence of the linear operator on τ. It is equally possible to formulate the problem in the x, τ plane and write the base profiles as functions of time. The former approach is used here.

Since the base state is time-dependent, the time at which the perturbation is introduced, $\tau = \tau_0$, acts as a parameter and influences the fate of the perturbation evolution. Furthermore, the initial conditions of the perturbation fields (at τ_0) are chosen to correspond to the eigenmodes of an auxiliary QSSA calculation (Tan & Homsy 1986). This helps us chose appropriate values of the wavenumber m, for fixed R and M, in the forward integration of the equations. The initial conditions are immaterial in the optimized solutions, since the form of the initial condition is selected by maximization of a cost function. Otherwise, QSSA is not investigated here in any detail since we carry out full time-dependent integration of the linearized stability equations.

920 A26-8

For the numerical implementation, the same spatial discretization is used for both base states and perturbation fields (as described in § 3.1), where we specify large enough domain size such that the perturbation fields decay sufficiently at both $\eta = \pm d$, in order to ensure that the boundary conditions are satisfied. The implicit second-order Crank–Nicolson time-marching method is employed for this linearized problem. However, as is typical in variable-density flows in the zero-Mach-number limit, there is no evolution equation for pressure. Hence, we use temporal staggered grid, where the velocity and scalar fields are defined at full time steps n and $n + 1$, while the pressure is assumed to be defined at the intermediate (staggered) time step $n + 1/2$ (Lu & Pantano 2020). The conservation of mass is then satisfied at the next time level $n + 1$. To this end, the Schur complement reduction is applied to solve for the pressure field first, followed by velocity and scalar fields. Details of the implementation are described in Appendix A.

Previous studies (Tan & Homsy 1986; Doumenc *et al.* 2010; Daniel *et al.* 2013) indicate that the maximum amplification gain of perturbation at a certain time τ_1 depends on the definition of the disturbance energy, which in general is given by

$$E(\tau_1) = \int_{-\infty}^{\infty} \{A_1[\hat{U}(\eta, \tau_1)^2 + \hat{V}(\eta, \tau_1)^2 + \hat{W}(\eta, \tau_1)^2] + A_2\hat{Y}(\eta, \tau_1)^2\}\,d\eta, \quad (3.16)$$

where the values of constants A_1 and A_2 control the choice of objective function, i.e. whether the quantity to be maximized is the kinetic energy, potential energy or total (kinetic and potential) energy. The normalized amplification factor is defined by

$$G(\tau_0; \tau_1) = \ln\left[\frac{E(\tau_1)}{E(\tau_0)}\right]^{1/2}, \quad (3.17)$$

where a subscript is attached to E and G to denote which particular cost function/disturbance energy is used, i.e. K $(A_1 = 1, A_2 = 0)$, Y $(A_1 = 0, A_2 = 1)$ and T $(A_1 = 1, A_2 = 1)$ to denote kinetic, potential and total, respectively. Note that $E_T = E_K + E_Y$. The amplification gain can be maximized using an adjoint optimization scheme, in which $E(\tau_1)$ is maximized subject to the constraint $E(\tau_0) = 1$ (Schmid & Henningson 2001; Schmid 2007). The augmented Lagrangian $\mathcal{L}$ of $E(\tau_1)$ is then defined by

$$\mathcal{L}(\lambda, \hat{\boldsymbol{\Psi}}, \hat{\boldsymbol{\Psi}}^+) = E(\tau_1) - \lambda[E(\tau_0) - 1] - \int_{\tau_0}^{\tau_1}\int_{-\infty}^{\infty} \hat{\boldsymbol{\Psi}}^+\mathcal{M}(\hat{\boldsymbol{\Psi}})\,d\eta\,d\tau, \quad (3.18)$$

where λ and $\hat{\boldsymbol{\Psi}}^+$ are the Lagrange multipliers, and $\hat{\boldsymbol{\Psi}}^+ = (\hat{U}^+, \hat{V}^+, \hat{W}^+, \hat{Y}^+, \hat{P}^+)$, referred to here as the adjoint variables. The constraint $\mathcal{M}(\hat{\boldsymbol{\Psi}})$ is given by (3.15). In order to determine first-order optimal conditions, the first variation of the Lagrangian,

$$\delta\mathcal{L}(\lambda, \hat{\boldsymbol{\Psi}}, \hat{\boldsymbol{\Psi}}^+) = \delta E(\tau_1) - \lambda\,\delta E(\tau_0) - \int_{\tau_0}^{\tau_1}\int_{-\infty}^{\infty} \delta\hat{\boldsymbol{\Psi}}^+\mathcal{M}(\hat{\boldsymbol{\Psi}})\,d\eta\,d\tau$$

$$- \int_{\tau_0}^{\tau_1}\int_{-\infty}^{\infty} \hat{\boldsymbol{\Psi}}^+\delta\mathcal{M}(\hat{\boldsymbol{\Psi}})\,d\eta\,d\tau, \quad (3.19)$$

must vanish. Some boundary integrals emerge when calculating the partial derivatives of $\mathcal{L}$, resulting in

$$
\int\limits_{\tau_0}^{\tau_1} \left\{ \frac{Sc\mu_0 Z_0}{4\tau} \left(2\frac{\partial \hat{U}}{\partial \eta}\hat{U}^+ + \frac{\partial \hat{V}}{\partial \eta}\hat{V}^+ + \frac{\partial \hat{W}}{\partial \eta}\hat{W}^+ + \frac{1}{Sc}\frac{\partial \hat{Y}}{\partial \eta}\hat{Y}^+ \right) - \frac{BZ_0}{\sqrt{\tau}}\hat{P}\hat{U}^+ \right.
$$

$$
\left. + \frac{(R-1)\mu_0}{4\tau}\frac{\partial \hat{Y}}{\partial \eta}\hat{P}^+ \right\} \Bigg|_{-\infty}^{+\infty} \, \mathrm{d}\tau = 0, \quad \text{where } B \equiv Sc\sqrt{K/8}, \tag{3.20}
$$

which is satisfied by imposing homogeneous boundary conditions as $\eta \to \pm\infty$. Finally, the optimality conditions are met if the following coupling conditions are satisfied:

$$
2[A_1(\hat{U}\delta\hat{U} + \hat{V}\delta\hat{V} + \hat{W}\delta\hat{W}) + A_2\hat{Y}\delta\hat{Y}]|_{\tau_1}
$$
$$
= [A_1(\hat{U}^+\delta\hat{U} + \hat{V}^+\delta\hat{V} + \hat{W}^+\delta\hat{W}) + A_2\hat{Y}^+\delta\hat{Y}]|_{\tau_1}, \tag{3.21a}
$$

$$
2\lambda[A_1(\hat{U}\delta\hat{U} + \hat{V}\delta\hat{V} + \hat{W}\delta\hat{W}) + A_2\hat{Y}\delta\hat{Y}]|_{\tau_0}
$$
$$
= [A_1(\hat{U}^+\delta\hat{U} + \hat{V}^+\delta\hat{V} + \hat{W}^+\delta\hat{W}) + A_2\hat{Y}^+\delta\hat{Y}]|_{\tau_0}. \tag{3.21b}
$$

Specifically, when maximizing the total energy, the coupling conditions are given by

$$
2\hat{X}|_{\tau_1} = \hat{X}^+|_{\tau_1}, \quad 2\lambda\hat{X}|_{\tau_0} = \hat{X}^+|_{\tau_0}, \tag{3.22a,b}
$$

where $\hat{X}^+ = (\hat{U}^+, \hat{V}^+, \hat{W}^+, \hat{Y}^+)$. On the other hand, when the kinetic (potential) energy is to be maximized, we have the coupling conditions only for velocities (scalar) while the scalar (velocities) are set to zero at τ_0 and τ_1 for both direct and adjoint variables. In the end, this leads to the adjoint optimization problem of the form

$$
\frac{\partial \hat{X}^+}{\partial \tau^+} = L^+(Sc, R, M, k, m, \tau^+)\hat{X}^+. \tag{3.23}
$$

The adjoint equations are to be integrated backwards in time. The detailed expressions of (3.23) and the operator L^+ are documented in Appendix A. First, we perform forward (direct) integration in time from τ_0 to τ_1, utilizing the normalized QSSA eigenmodes as our initial conditions. In order to prevent too large a round-off error, we determine that τ_1 is the time at which $G \approx 7$. At τ_1, we integrate the adjoint governing equations backwards in time from τ_1 to τ_0 with the homogeneous boundary conditions. The initial conditions for adjoint integration depend on the coupling conditions, (3.21). The numerical implementation is identical to that of forward integration, but using adjoint equations and initial and boundary conditions instead. The above procedure is iterative, and we determine convergence between two iterations as when $|G^n(\tau_1) - G^{n-1}(\tau_1)| \leqslant 10^{-6}$.

4. Results

Prathama & Pantano (2017) carried out the inviscid analysis of this flow configuration and determined that the interface was unconditionally unstable, even in the presence of surface tension. They give the inviscid interface amplitude $\tilde{\zeta}(\tilde{\tau})$ as a function of the inviscid time $\tilde{\tau}$ by

$$
\tilde{\zeta}(\tilde{\tau}) = C_1 D_{-1/2}(\tilde{\tau}) + C_2 D_{-1/2}(\mathrm{i}\tilde{\tau}) \sim \mathrm{e}^{\tilde{\tau}^2/4}\tilde{\tau}^{-1/2} \quad \text{(for large } \tilde{\tau}), \tag{4.1}
$$

where $D_j(z)$ is the parabolic cylinder function of order j and C_1 and C_2 are constants shown in Appendix B and correspond to an interface that starts its evolution at $\tau = \tau_0$ when

920 A26-10

$\Delta w_0 \neq 0$; the values of the constants reported in Prathama & Pantano (2017) correspond to the initial condition at $\tau = 0$, which is not relevant here. The inviscid time is related to the non-dimensionalized time τ according to

$$\tilde{\tau} = \left[\frac{m(R-1)}{\sqrt{R}} \right]^{1/2} \tau, \qquad (4.2)$$

where m is the non-dimensional wavenumber defined by the scaling in (2.7b). The normalized amplification factor of the inviscid case is given by

$$G_{inv}(\tilde{\tau}) = \ln \left[\frac{E_Y(\tilde{\tau})}{E_Y(\tilde{\tau}_0)} \right]^{1/2} = \frac{1}{2} \ln[\tilde{\zeta}(\tilde{\tau})], \qquad (4.3)$$

with $\tilde{\zeta}(\tilde{\tau}_0) = 1$ as the initial condition. The inviscid asymptotic growth, using (4.1), behaves as $G_{inv} \sim (\tilde{\tau} - \tilde{\tau}_0)^2/8 = (m(R-1)/8\sqrt{R})(\tau - \tau_0)^2$. In practice, this amplification factor is so large that usually one does not reach this large-time regime before the LSA becomes invalid. Furthermore, the inviscid analysis also showed that purely two-dimensional perturbations ($k = 0$) are more unstable, for any given vertical wavenumber m, than at any other three-dimensional perturbation that has $k \neq 0$. In subsequent discussions, the Schmidt number is unity in all cases, which is appropriate for understanding mixing of two typical gaseous fluids. But it is acknowledged that this is less so for liquids where each column may have substantially different diffusivities; a modification of the present analysis is required for this situation.

Contrary to the inviscid case where all wave modes are unstable, the behaviour of the viscous case is expected to depend on the value of m. The QSSA approach, which has limited accuracy in this strongly time-dependent problem, is used here to determine meaningful values of m for some interface parameters of interest. First, we choose $R = 5$ and $M = 1$ to focus on a particular case of reasonable interest of mixing of gases with contrasting densities; e.g. an air–SF_6 interface (commonly used in experiments) has $R = 5.036$ at 1 atm. Furthermore, we can interpret that τ_0 is related to the so-called early-time Reynolds number, Re_0, which describes the instantaneous base state condition when the flow is perturbed by infinitesimal disturbances, and can be expressed as

$$Re_0 = \frac{\Delta w_0 \delta_0}{\bar{\nu}} \approx \frac{g t_0 \sqrt{\bar{\nu} t_0}}{\bar{\nu}} = \frac{g}{\sqrt{\bar{\nu}}} (T\tau_0)^{3/2} = \frac{g}{\sqrt{\bar{\nu}}} \left(\frac{\bar{\nu}^{1/3}}{g^{2/3}} \tau_0 \right)^{3/2} = \tau_0^{3/2}, \qquad (4.4)$$

where the velocity difference between the two streams is $\Delta w_0 \sim g t_0$ and the thickness of the interface is $\delta_0 \sim \sqrt{\bar{\nu} t_0}$. Therefore, initially we choose to concentrate on results for $\tau_0 = 10$ corresponding to $Re_0 \sim 32$, to explore the dynamics of the perturbations and perform a subsequent parametric study to investigate results for a wider range of τ_0. The wavenumber of peak amplification according to the QSSA is $m_{peak} = 0.625$ and the neutral wavenumber is $m_{neutral} = 0.148$ for $\tau_0 = 10$ from the data shown in figure 16. Consequently, we first focus on evaluating the impact of the energy function choice, (3.16), used to measure amplification of the perturbations at a wavenumber close to m_{peak}, i.e. $m = 0.05$ (easy to recall).

4.1. *Two-dimensional perturbations*

First, we consider moderate wavenumbers m and purely two-dimensional perturbations, i.e. $k = 0$, because the numerical solutions indicate that these perturbations are more unstable than three-dimensional perturbations, i.e. $k \neq 0$. Three-dimensional perturbations
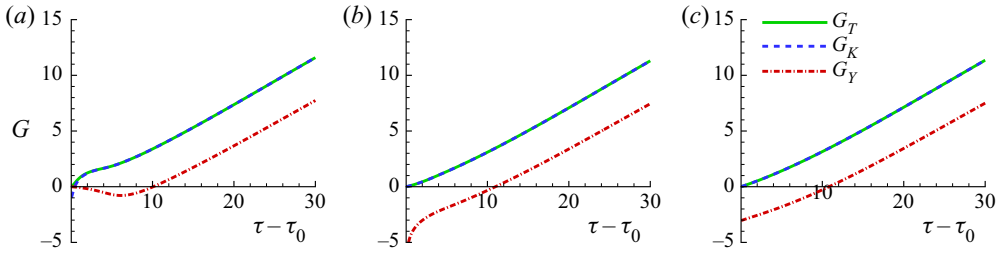
Figure 4. Amplification factors G_T, G_K and G_Y with different initializations of $E_Y(\tau_0) = 1$ (a), $E_K(\tau_0) = 1$ (b) and $E_T(\tau_0) = 1$ (c) for $R = 5$, $M = 1$, $\tau_0 = 10$, $m = 0.05$ and $k = 0$ (two-dimensional).
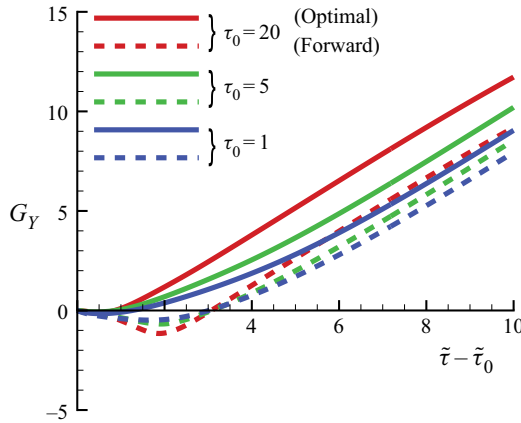

Figure 5. The E_Y-optimal (solid) versus forward (dashed) amplification factors for $R = 5$, $M = 1$, $m = 0.05$ and $\tau_0 = 1$, 5 and 20.

are investigated in the next section for conditions close to the neutral amplification regime. Figure 4 shows forward integration (non-optimized) amplification factors for $R = 5$, $M = 1$, $\tau_0 = 10$, at the wavenumber $m = 0.05$. The initial conditions were chosen to be: $\hat{U} = \hat{W} = 0$ and $\hat{Y} = \hat{Y}^{QSSA}$ (figure 4a), $\hat{U} = \hat{U}^{QSSA}$, $\hat{W} = \hat{W}^{QSSA}$ and $\hat{Y} = 0$ (figure 4b) and both velocity and scalar eigenfunctions from QSSA (figure 4c). It is seen that G_K and G_T are almost indistinguishable because the amount of energy in the scalar Y is typically very small, in comparison with the kinetic energy. But, note that all curves (after some initial transient) evolve similarly as time grows. It is worth mentioning that figure 4(a) shows that the scalar energy E_Y can decay initially when the flow velocity is initialized to zero. This is caused by diffusional decay of the scalar perturbations since there is little flow at early times. The decay of solutions with time was indeed observed in the DNS of Gat *et al.* (2017), which manifests early on because pure convective processes start driving the instability only at later times. This can be seen by expanding (4.1) (inviscid behaviour) for small $\tilde{\tau}$, resulting in

$$\hat{\zeta}(\tilde{\tau}) = 1 + \tfrac{1}{48}\tilde{\tau}^4 + O(\tilde{\tau}^8), \tag{4.5}$$

which indicates that there is substantial time, up to $\tilde{\tau} \sim 48^{1/4} \approx 2.6$, for viscous effects to be felt. Note that the minimum of G_Y where perturbations start to grow again happens at $\tilde{\tau} \sim 2$; see figure 5, where we plot as a function of $\tilde{\tau}$ both non-optimized and E_Y-optimized solutions for $R = 5$, $M = 1$, $m = 0.05$ and three values of τ_0: 1, 5 and 20.
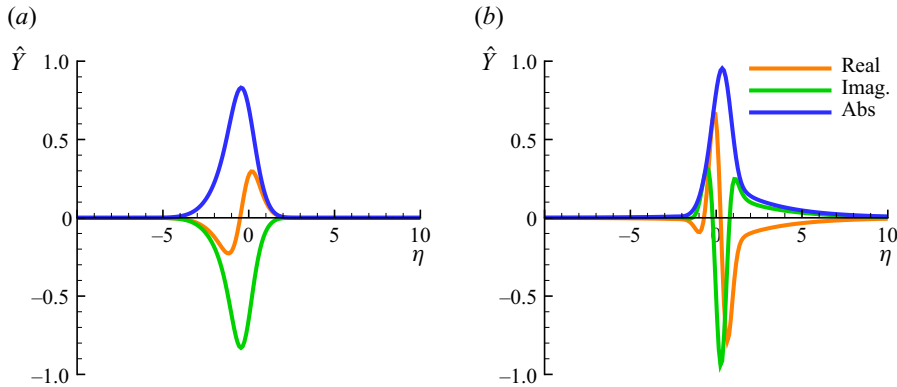
920 A26-12

Figure 6. Comparison between forward (*a*) and E_Y optimal (*b*) initial conditions of $\hat{Y}$ for $R = 5$, $M = 1$, $m = 0.05$ and $\tau_0 = 20$.

From figure 5, we can see that optimal perturbations which maximize E_Y tend to choose initial perturbations that minimize this initial decay. This feature disappears, though, when the velocity is also initialized to be non-zero, as shown in figure 4(*b*,*c*). Figure 6 displays the optimized initial conditions as compared with those from QSSA, for $\tau_0 = 20$. It is evident that the optimal solutions exhibit a shortened initial diffusional dampening phase and that the optimal scalar profiles seem to be more compressed, which are better at extracting energy from the mean shear (Foures, Caulfield & Schmid 2014).

Subsequently, we concentrate on the optimal growth rates that maximize the total energy function, E_T. Figure 7 shows the optimized amplification factor G_T for $R = 5$, $M = 1$ at wavenumbers $m = 0.01$ and 0.05. At $m = 0.01$ (figure 7*a*), the amplification factor increases with growing τ_0, as expected based on the relationship between τ_0 and the early Reynolds scaling, (4.4). Interestingly, at the higher wavenumber $m = 0.05$ (figure 7*b*), the growth rate is not monotonic with increasing τ_0, where solutions reverse half way from growth to decay. This is not observed in the QSSA since $\omega_I > 0$ for all τ_0 cases considered here (see figure 16*c*) suggesting that the spreading of the base profile with time is sufficiently strong to modify the qualitative behaviour substantially space between words. Further inspection of the perturbation equations for small τ_0 (see Appendix A) suggests that: (i) initially, the dominant terms are the ones involving Y_0 (equivalently, Z_0) and its derivatives (potential energy), yet (ii) at later times, the terms involving W_0 (shear) and viscous dissipation (approximately proportional to m^2) are dominant, although these effects increase slowly.

Figure 8 shows a comparison between the optimal amplification factors (solid lines) at small wavenumber, $m = 0.01$, and their inviscid counterparts (dashed lines) for large τ_0, plotted in terms of the inviscid time, (4.2). The inviscid curves are given by using the exact (4.1) in (4.3). We can observe that the viscous solutions become closer to the inviscid result as τ_0 grows, corresponding to larger Re_0, (4.4), suggesting that we retrieve the inviscid result asymptotically.

Finally, figure 9(*a*) shows the optimal amplification factors as a function of density ratio at $M = 1$, $m = 0.05$ and $\tau_0 = 10$. It can be observed that the least stable case is $R = 10$ since high density ratio relates to a stronger potential energy of the columns that feed into the instability, also promoting growth of the mixing layer between the two columns. Interestingly, the growth rate for the $R = 7.5$ case is very close to that for the $R = 10$ case, suggesting that the influence of density ratio saturates. Figure 9(*b*) exhibits the optimal
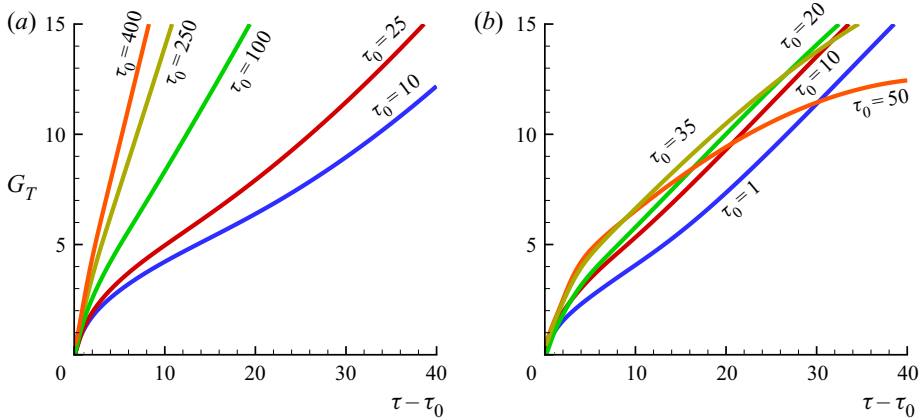
Figure 7. The E_T-optimized amplification factors as functions of τ_0 for $R = 5$, $M = 1$ and $m = 0.01$ (*a*) and $m = 0.05$ (*b*).
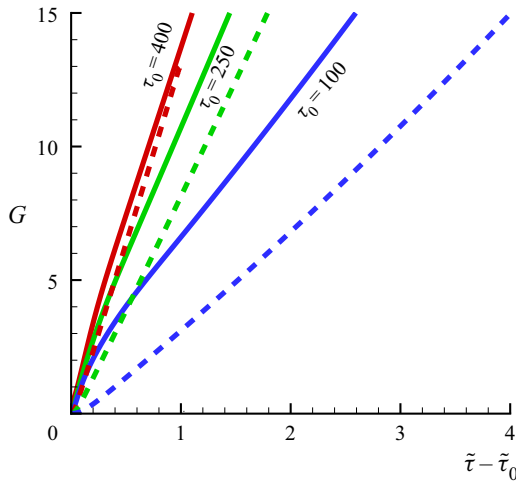

Figure 8. Optimal G_T (solid) versus their corresponding inviscid G_{inv} (dashed) amplification factors for $R = 5$, $M = 1$ and $m = 0.01$.

amplification factors as a function of M at $R = 5$, $m = 0.05$ and $\tau_0 = 10$. The early-time behaviours are indistinguishable for all cases, but as viscous effects become dominant at later times, we can see that the flow is least stable when the displacing (heavier) fluid is less viscous than the displaced fluid, i.e. $M = 1/4$. This behaviour is also observed in other studies of variable-viscosity miscible fluids (Riaz, Pankiewitz & Meiburg 2004; Kim & Choi 2011; Etrati, Alba & Frigaard 2018), where significant flow destabilization is a consequence of the peak of the eigenfunctions tending to shift towards the less viscous fluid region. Hence the driving kinetic energy of the heavier fluid is less damped and this unfavourable viscosity difference renders the flow more unstable.

This section concludes with a brief description of the physical features of the perturbation fields. Figure 10 displays the optimal perturbation fields of a typical growing disturbance for $R = 5$, $M = 1$, $m = 0.05$ and $\tau_0 = 10$, at initial time τ_0 and at the time $\tau \approx 31.6$ when $G_T \approx 10$. The perturbation fields are characterized by flow patterns that

920 A26-14

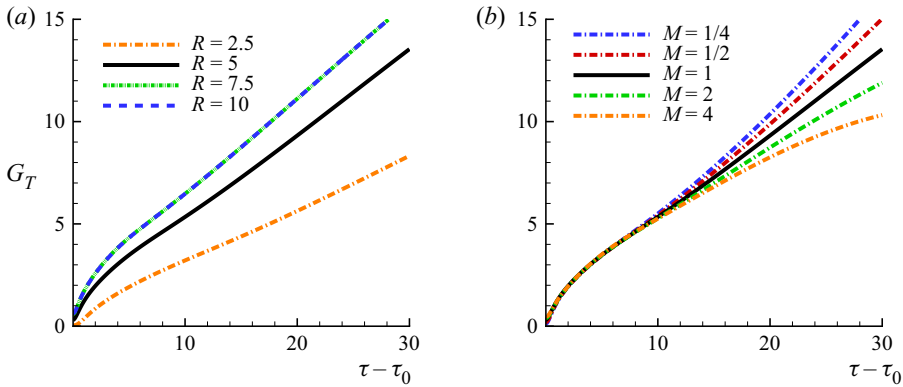Figure 9. Optimal amplification factors for $m = 0.05$, $\tau_0 = 10$ as a function of R with uniform viscosity $M = 1$ (a) and as a function of M with density ratio $R = 5$ (b).
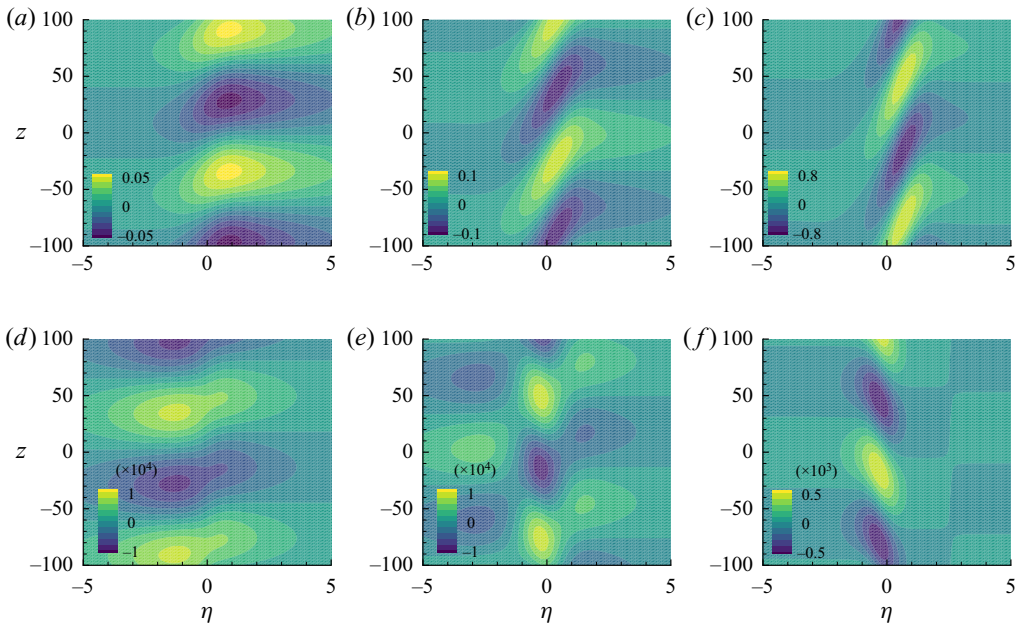

Figure 10. Two-dimensional optimal perturbation fields u_1 (a,d), w_1 (b,e) and Y_1 (c,f) at initial time τ_0 (a–c) and at time ($\tau = 31.64$) when $G_T \approx 10$ (d–f) of typical growing disturbance for $R = 5$, $M = 1$, $m = 0.05$ and $\tau_0 = 10$.

are tilted against the base-flow shear, which persists throughout the linear amplification region considered here. This misalignment facilitates efficient energy transfer from the base flow to the perturbation (Farrell 1988; Schmid & Henningson 2001; Foures *et al.* 2014). As time increases, the peak of u_1 shifts from the heavier (right) to the lighter (left) fluid region. Furthermore, the peaks of w_1 seem no longer concentrated around $\eta = 0$, but have developed more local peaks adjacent at both sides of the core mixing layer. Finally, both w_1 and scalar fields have changed their orientation and are now tilted opposite to their original alignments.
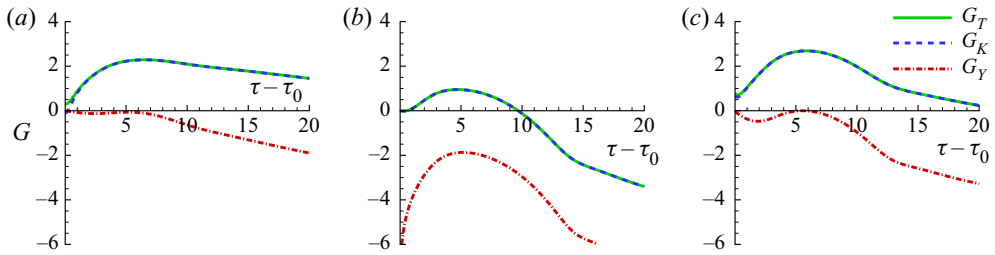
Figure 11. Optimal amplification factors G_T, G_K and G_Y with different cost functions E_Y (*a*), E_K (*b*) and E_T (*c*) for $R = 5$, $M = 1$, $\tau_0 = 10$, $m = 0.16$ and $k = 0.05$.

4.2. *Three-dimensional perturbations*

In this section we consider conditions close to the neutral amplification wavenumber where the perturbations are not expected to grow. The QSSA indicates that this happens at $m_{neutral} = 0.148$ for $R = 5$, $M = 1$ and $\tau_0 = 10$. Therefore, we choose $m = 0.16$, slightly higher than $m_{neutral}$, and first investigate the influence of different objective functions for fixed k. Figure 11 shows comparisons of the different amplification factors for $k = 0.05$ and optimized solutions with cost functions E_Y, E_K and E_T. Generally, we observe that G_T (also G_K) is larger than G_Y, as before, but interestingly G_T (also G_K) displays transient growth for all types of cost function optimization (Butler & Farrell 1992; Schmid & Henningson 2001; Kaminski *et al.* 2014). The peak of this transient growth happens at approximately the same time (for different optimization functions) but the decay is substantially slower when using E_Y, followed by E_T and much faster when using E_K. Evidently, the intermediate decay displayed by the E_T optimization is a combination of the effects of purely optimizing on the scalar variance E_Y (slower decay) and the kinetic energy of the flow E_K (faster decay). The curves of G_Y for all these cases show also transient behaviour but of different nature. When optimizing for E_Y and E_T (figure 11*a*,*c*), we observe an initial decay of the scalar variance, which was attributed earlier to diffusion. After this decay, which is not observed when optimizing E_K, there is transient growth towards a peak, followed by decay. In the optimized solutions using E_Y and E_T, the scalar amplification factor never exceeds the initial scalar variance.

Now, we concentrate on optimized solutions with the total energy cost function, E_T, since it encompasses both flow and scalar behaviour. Figure 12 displays the evolution of G_T for different values of the spanwise wavenumber k. First, it is apparent that there is short-term transient growth at all k plotted, with $G_{T,max}$ larger than that of the purely two-dimensional mode $k = 0$. This can be attributed to the lift-up effect of fluid elements in shear flows (Schmid & Henningson 2001). The behaviour of $G_{T,max}$ is not monotonic with k, however. Factor $G_{T,max}$ increases with increasing k up to $k \approx 0.1$, followed by a decrease of the amplification factor for larger k. All perturbations eventually decay, with the two-dimensional mode experiencing the slowest rate of decay at large times, which indicates that three-dimensional modes are slightly more important early on during the evolution. Note that the differences in amplification factors are not large for all values of k shown.

Figure 13 shows the optimal perturbation fields for the two-dimensional case (corresponding to the black curve in figure 12) of $R = 5$, $M = 1$, $m = 0.16$ and $\tau_0 = 10$, at initial time τ_0 and at the time ($\tau = 15.52$) when maximum amplification is reached: $G_{T,max} \approx 2.53$. As seen before at lower m, initially the flow patterns are tilted slightly against the base-flow shear but, as time progresses, the disturbances eventually rotate to
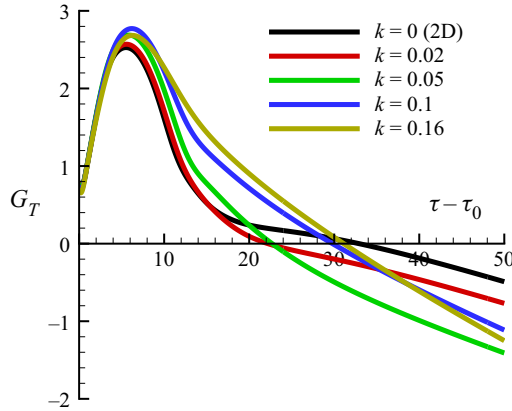
Figure 12. The E_T-optimal amplification factors for $R = 5$, $M = 1$, $\tau_0 = 10$ and $m = 0.16$, and different values of k.

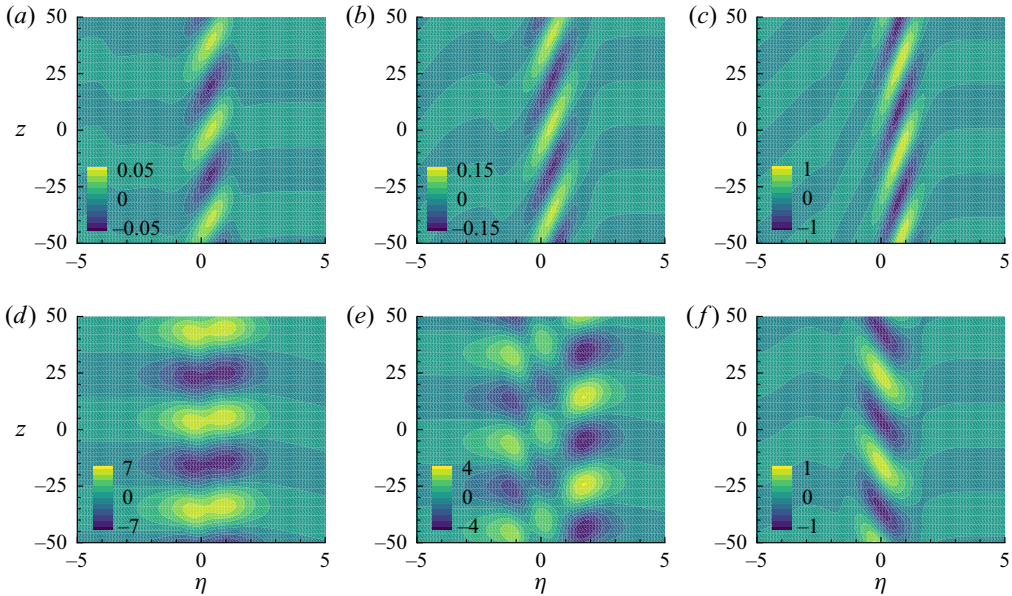Figure 13. Two-dimensional ($k = 0$) optimal perturbation fields u_1 (a,d), w_1 (b,e) and Y_1 (c,f) at initial time τ_0 (a–c) and at time ($\tau = 15.52$) when $G_{T,max} \approx 2.53$ (d–f) for $R = 5$, $M = 1$, $m = 0.16$ and $\tau_0 = 10$.

become more aligned with the mean shear direction and cause transient growth of energy, also known as the Orr mechanism (Schmid & Henningson 2001). Overall, the behaviour is similar to that displayed by the perturbations at lower m in figure 10.

Finally, figure 14 shows the optimal perturbation fields for a three-dimensional case (corresponding to the green curve in figure 12) of $R = 5$, $M = 1$, $k = 0.05$, $m = 0.16$ and $\tau_0 = 10$, at the initial time (figure 14a,c,e,g) and at the time ($\tau = 15.88$) when maximum amplification is reached (figure 14b,d,f,h): $G_{Y,max} \approx 2.69$. The perturbation patterns are similar to those of figure 13 except that the oblique structure of the mode is now evident. The presence of a spanwise component of perturbation v_1 is also worth mentioning, and noticing that it has magnitude similar to that of u_1.
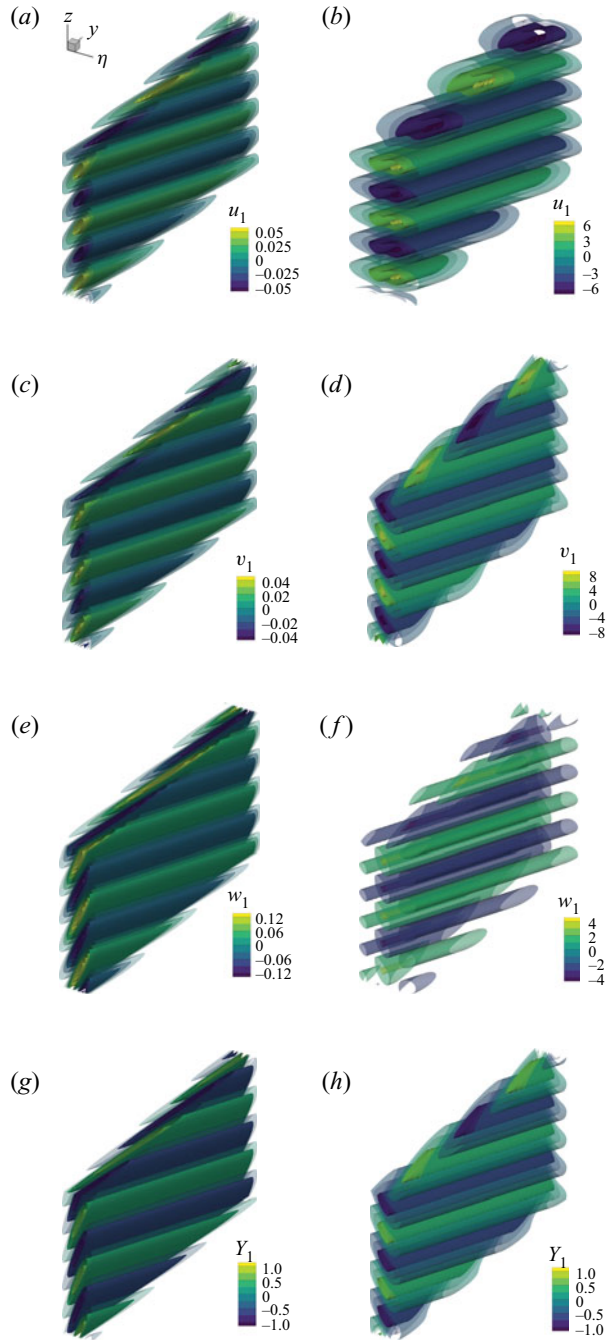
Figure 14. Three-dimensional optimal perturbation fields u_1, v_1, w_1 and Y_1 at $\tau_0 = 10$ (a,c,e,g) and $\tau = 15.88$ (b,d,f,h) for $R = 5$, $M = 1$, $k = 0.05$ and $m = 0.16$.
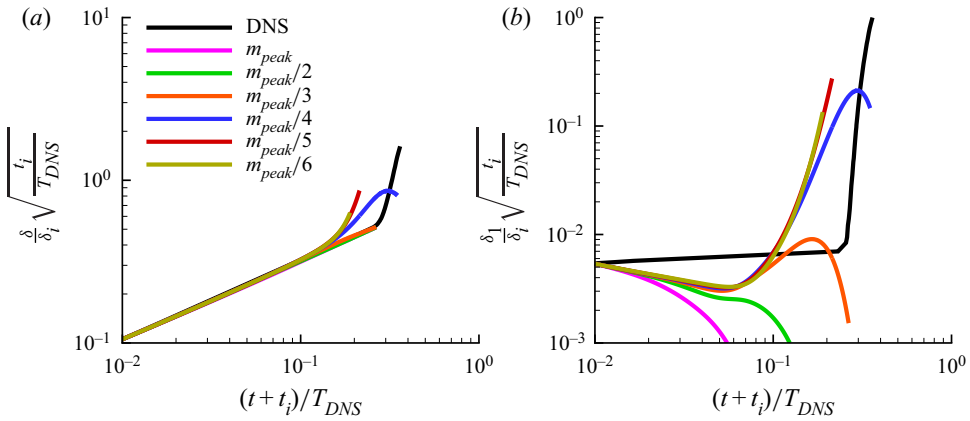
Figure 15. Temporal evolution of the shear-layer width $(\delta/\delta_i)\sqrt{t_i/T_{DNS}}$ including the base profile (*a*), and perturbation width excluding the base profile $(\delta_1/\delta_i)\sqrt{t_i/T_{DNS}}$ (*b*) for forward integrations with $R = 5$, $M = 1$, $\tau_0 = 1.12$ and several values of m, compared against DNS result taken from Gat *et al.* (2017).

5. Comparison with DNS

The DNS study carried out by Gat *et al.* (2017) considered uniform viscosity, $M = 1$, for several density ratios R. They analysed the behaviour of the thickness of the interface with time and other nonlinear statistics not covered in this study. Figure 15 displays the evolution of the shear-layer width, which indicates that there are two mixing-layer temporal evolution regimes: an initial diffusion-dominant regime with growth rate $\sim \sqrt{\tau}$, followed by a turbulence-dominated regime with growth rate $\sim \tau^3$. The early-time growth corresponds to viscous spreading contained in the base (self-similar) profiles, whereas the growing disturbances which dominate the base flows promote much faster growth at later times, as described below.

In order to compare the DNS results with LSA, first one needs to translate the parameters of their initial conditions to the present variables. Defining the initial shear-layer thickness δ_i as the width at which $0.1 < Y < 0.9$ at initial time t_i, from figure 3(*b*) of Gat *et al.* (2017) we obtain $\delta_i \approx 0.02\ell = 0.13$ for $R = 5$, where $\ell = 2\pi$. Meanwhile, this corresponds to $\Delta\eta \approx 2.96$ in our self-similar Y_0 profile in figure 2. By using (2.7*b*) and (3.2), we can determine their initial (start-up) time, given in our non-dimensional units by

$$\tau_0 = \left(\frac{\delta_i/L}{\Delta\eta}\right)^2 \frac{1}{2K} = \left[\frac{\delta_i/(\bar{v}^2 g^{-1})^{1/3}}{\Delta\eta}\right]^2 \frac{RSc}{2(R+1)} = \left[\frac{0.13/(0.0044^{2/3})}{2.96}\right]^2 \frac{5}{12} = 1.12,$$
(5.1)

for their given $\mu = 0.0044$ and $g = 1$. Secondly, we need to match their perturbation wavenumber to our m. From figure 15(*a*) in Gat *et al.* (2017), for 'Pert3' on 1024^3 grid, the dimensionless wavenumber corresponding to the peak of the perturbation spectrum is $k_r \Delta x \approx 0.15$, which yields $k_r \approx (0.15)(1024)/(4\pi) = 12.22$, since their domain size is 4π. We non-dimensionalize this result to obtain our $m_{peak} = k_r L = (12.22)(\bar{v}^2 g^{-1})^{1/3} = 0.33$. Subsequently, we carry out forward integration for $R = 5$, $M = 1$, $\tau_0 = 1.12$ for several wavenumbers, starting from m_{peak} down to its sixth subharmonics. Figure 15 shows the temporal evolutions of the shear-layer thickness δ (figure 15*a*) and the width of the perturbation δ_1 (figure 15*b*) compared against the DNS from Gat *et al.* (2017).

The horizontal axis is scaled with the time scale used in their simulation, T_{DNS}, given by

$$T_{DNS} = 2\pi \sqrt{\frac{\ell}{\mathcal{A}g}} = 19.29, \quad \text{where } \mathcal{A} = \frac{R-1}{R+1} = \frac{2}{3} \quad \text{for } R = 5. \qquad (5.2)$$

We observe that the transition from viscous decay to rapid growth happens at $(t + t_i)/T_{DNS} \approx 0.1$. This is comparable with the transition times observed in the DNS given by $(t + t_i)/T_{DNS} \approx 0.25$. The slightly earlier transition time predicted by LSA owes its origin to the initial condition used in the linearized study, which is obtained from the eigenmodes of the QSSA analysis, since these modes are more unstable than the random two-dimensional field, with a wide spectrum, used in the DNS. Despite this difference, the agreement is quite good and helps to connect the linear and nonlinear studies. It appears that the peak wave mode chosen space between words in the DNS was not an amplifying one, and instead the instability was triggered by lower wave modes present in the initial condition.

6. Conclusion

The LSA of two fluid columns with different densities and viscosities in a gravitational field has been investigated and compared with previous inviscid analysis. In this configuration, a uniform gravity field acts in the direction transverse to the density stratification, resulting in opposing constant acceleration of the free streams. We perform numerical integration of the linear time-dependent IVP as a function of wavenumber. Furthermore, we carry out adjoint optimization in order to determine the initial profiles that result in maximum amplification at a finite time horizon. Within the strongly unstable range of wavenumbers, we confirm that the evolution approaches the inviscid limit as the initial Reynolds number of the flow increases. In this regime, the two-dimensional mode is the most unstable (dominant). At higher wave modes, around the region of neutral stability, it is found that transient growth is present and that three-dimensional modes (with a spanwise non-zero wavenumber) are more unstable than the two-dimensional mode. The difference in amplification factors between two- and three-dimensional modes is not very large, but it is noticeable.

We also investigated the effect of different optimization cost functions and concluded that using the total energy of the flow, kinetic and potential, gives an overall picture of the evolution. Using a cost function based only on scalar variance (potential energy) highlights initial transients of the mixture fraction that are controlled by diffusion. Optimization of the initial scalar profiles can largely remove this diffusional decay from the dynamics but hides flow effects (velocity) that are important overall.

Declaration of interests. The authors report no conflict of interest.

Author ORCIDs.
Ⓓ Aditya Heru Prathama https://orcid.org/0000-0002-2207-3011;
Ⓓ Carlos Pantano https://orcid.org/0000-0003-3971-2278.

Appendix A. Detailed perturbation equations

A.1. *Linear IVP – forward equations*

The forward equations for the first-order perturbation fields are

$$
\frac{\partial \hat{U}}{\partial \tau} = \frac{Sc\mu_0 Z_0}{2\tau} D^2 \hat{U} + \left\{ \frac{[(R-1)\mu_0 + 2\beta ScZ_0]Y_0' + 2\eta}{4\tau} \right\} D\hat{U}
$$

$$
- \left[i(kV_0 + mW_0\tau) + \frac{(k^2+m^2)ScK\mu_0 Z_0}{2} - \frac{(R-1)(\mu_0 Y_0'' + \beta Y_0'^2)}{4\tau} \right] \hat{U}
$$

$$
+ \frac{ikB\mu_0 Z_0}{\sqrt{\tau}} D\hat{V} + \frac{imB\mu_0 Z_0}{\sqrt{\tau}} D\hat{W} - \frac{\beta(R-1)BZ_0(\mu_0 Y_0'' + \beta Y_0'^2)}{2\sqrt{\tau^3}} D\hat{Y}
$$

$$
+ \left[\frac{i(kV_0' + mW_0'\tau)\beta BZ_0}{\sqrt{\tau}} + \frac{(R-1)^2 B(\mu_0^2 Y_0''' + 4\beta\mu_0 Y_0' Y_0'' + \beta^2 Y_0'^3)}{4Sc\sqrt{\tau^3}} \right.
$$

$$
\left. - \frac{\beta(R-1)BZ_0(\mu_0 Y_0''' + 3\beta Y_0' Y_0'')}{2\sqrt{\tau^3}} \right] \hat{Y} - \frac{BZ_0}{\sqrt{\tau}} D\hat{P}, \tag{A1}
$$

$$
\frac{\partial \hat{V}}{\partial \tau} = \frac{ikB\mu_0 Z_0}{\sqrt{\tau}} D\hat{U} + \left(\frac{ik\beta BZ_0 Y_0'}{\sqrt{\tau}} - \frac{V_0'}{\sqrt{2K\tau}} \right) \hat{U} + \frac{Sc\mu_0 Z_0}{4\tau} D^2 \hat{V}
$$

$$
+ \left\{ \frac{[(R-1)\mu_0 + \beta ScZ_0]Y_0' + 2\eta}{4\tau} \right\} D\hat{V}
$$

$$
- \left[i(kV_0 + mW_0\tau) + \frac{(2k^2+m^2)ScK\mu_0 Z_0}{2} \right] \hat{V}
$$

$$
- \frac{kmScK\mu_0 Z_0}{2} \hat{W} + \frac{\beta ScZ_0 V_0'}{4\tau} D\hat{Y} + \frac{Sc\left[\beta Z_0 V_0'' - (R-1)\left(\mu_0 V_0'' + \beta V_0' Y_0'\right)\right]}{4\tau} \hat{Y}
$$

$$
- \frac{ikScKZ_0}{2} \hat{P}, \tag{A2}
$$

$$
\frac{\partial \hat{W}}{\partial \tau} = \frac{imB\mu_0 Z_0}{\sqrt{\tau}} D\hat{U} + \left(\frac{im\beta BZ_0 Y_0'}{\sqrt{\tau}} - \sqrt{\frac{\tau}{2K}} W_0' \right) \hat{U}
$$

$$
- \frac{kmScK\mu_0 Z_0}{2} \hat{V} + \frac{Sc\mu_0 Z_0}{4\tau} D^2 \hat{W} + \left\{ \frac{[(R-1)\mu_0 + \beta ScZ_0]Y_0' + 2\eta}{4\tau} \right\} D\hat{W}
$$

$$
- \left[i(kV_0 + mW_0\tau) + \frac{(k^2+2m^2)ScK\mu_0 Z_0}{2} \right] \hat{W} + \frac{\beta ScZ_0 W_0'}{4} D\hat{Y}
$$

$$
+ \left\{ \frac{Sc\left[\beta Z_0 W_0'' - (R-1)\left(\mu_0 W_0'' + \beta W_0' Y_0'\right)\right]}{4} - \frac{R^2-1}{2R} \right\} \hat{Y} - \frac{imScKZ_0}{2} \hat{P}, \tag{A3}
$$

$$\frac{\partial \hat{Y}}{\partial \tau} = -\frac{Y_0'}{\sqrt{2K\tau}}\hat{U} + \frac{\mu_0 Z_0}{4\tau}D^2\hat{Y} + \left\{ \frac{[(R-1)\,\mu_0 + 2\beta Z_0]\,Y_0' + 2\eta}{4\tau} \right\}D\hat{Y}$$

$$- \left[\mathrm{i}\,(kV_0 + mW_0\tau) + \frac{(k^2+m^2)K\mu_0 Z_0}{2} + \frac{(R-1)(\mu_0 Y_0'' + \beta Y_0'^2) - \beta Z_0 Y_0''}{4\tau} \right]\hat{Y}, \tag{A4}$$

$$\frac{1}{\sqrt{2K\tau}}D\hat{U} + \mathrm{i}k\hat{V} + \mathrm{i}m\hat{W}$$

$$+ (R-1)\left\{ \frac{\mu_0}{4\tau}D^2\hat{Y} + \frac{\beta Y_0'}{2\tau}D\hat{Y} + \left[\frac{\beta Y_0''}{4\tau} - \frac{(k^2+m^2)K\mu_0}{2} \right]\hat{Y} \right\} = 0, \tag{A5}$$

where the symbols D and primes denote η-derivatives. The equations above can be expressed in compact form as

$$\frac{\partial \hat{X}}{\partial \tau} = A\hat{X} + B\hat{P}, \tag{A6a}$$

$$C\hat{X} = 0, \tag{A6b}$$

where $\hat{X} = (\hat{U}, \hat{V}, \hat{W}, \hat{Y})$. Taking the derivative of (A6b) with respect to time, we have

$$\frac{\partial C}{\partial \tau}\hat{X} + C\frac{\partial \hat{X}}{\partial \tau} = 0, \tag{A7}$$

and substituting (A6a) yields the equation for pressure:

$$\hat{P} = -(CB)^{-1}\left(\frac{\partial C}{\partial \tau} + CA \right)\hat{X}. \tag{A8}$$

The pressure can be substituted back into (A6a) to obtain

$$\frac{\partial \hat{X}}{\partial \tau} = \left[A - B\,(CB)^{-1}\left(\frac{\partial C}{\partial \tau} + CA \right) \right]\hat{X} \equiv L\hat{X}. \tag{A9}$$

In the numerical implementation, after performing the spatial discretization (as described in § 3.1), the implicit second-order Crank–Nicolson time-marching method has the form of

$$\frac{\hat{X}^{n+1} - \hat{X}^n}{\Delta \tau} = \frac{1}{2}[\mathbb{A}^n \hat{X}^n + \mathbb{A}^{n+1} \hat{X}^{n+1}] + \mathbb{B}^{n+1/2} \hat{P}^{n+1/2}, \tag{A10a}$$

$$\mathbb{C}^{n+1} \hat{X}^{n+1} = 0, \tag{A10b}$$

where the block matrices $\mathbb{A}$, $\mathbb{B}$ and $\mathbb{C}$ are the discrete counterparts of those in (A6). Rearranging terms, we have

$$\begin{bmatrix} \mathbb{E} & \mathbb{F} \\ \mathbb{C} & 0 \end{bmatrix}\begin{bmatrix} \hat{X}^{n+1} \\ \hat{P}^{n+1/2} \end{bmatrix} = \begin{bmatrix} \mathbb{G}\hat{X}^n \\ 0 \end{bmatrix}, \tag{A11}$$
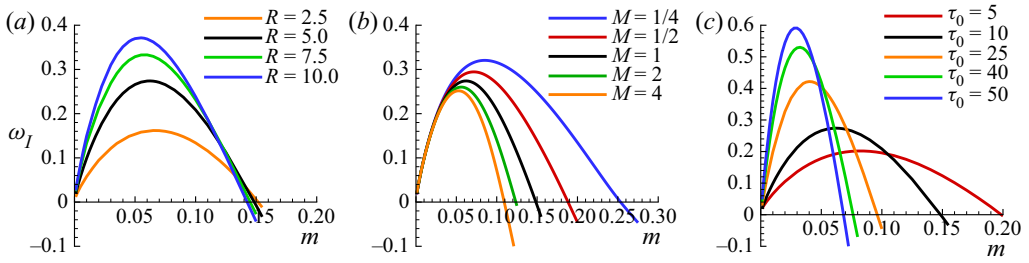
Figure 16. Imaginary frequency ω_I as (*a*) a function of R for $M = 1$ and $\tau_0 = 10$, (*b*) a function of M for $R = 5$ and $\tau_0 = 10$ and (*c*) a function of τ_0 for $R = 5$ and $M = 1$.
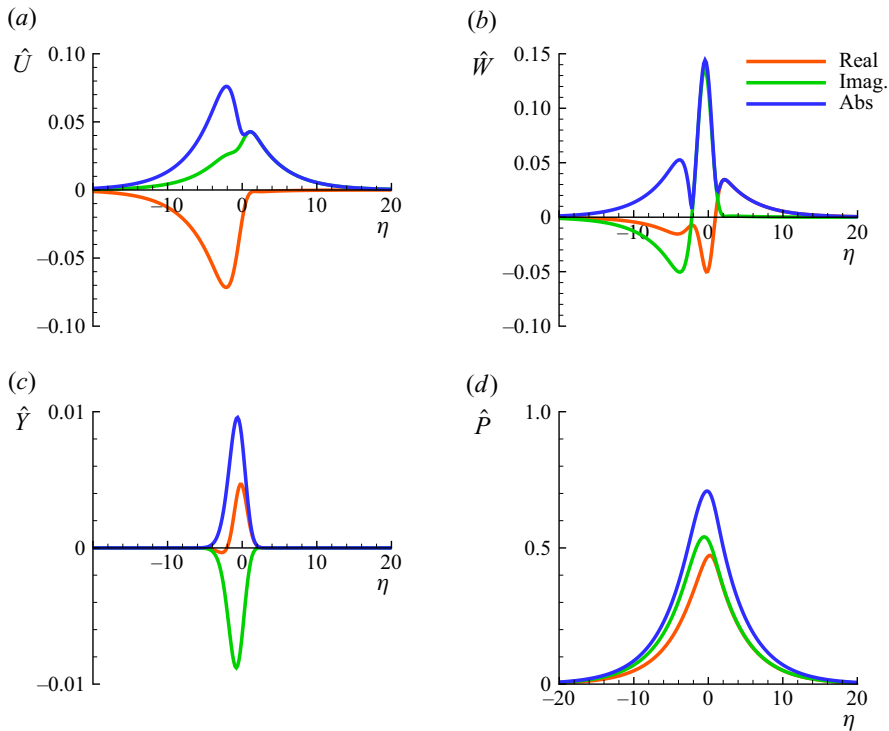

Figure 17. The eigenfunctions for $R = 5$, $M = 1$, $\tau_0 = 10$ and $m = 0.05$.

where $\mathbb{E} = (\mathbb{I} - \Delta\tau\mathbb{A}^{n+1}/2)$, $\mathbb{F} = (-\Delta\tau\mathbb{B}^{n+1/2})$, $\mathbb{G} = (\mathbb{I} + \Delta\tau\mathbb{A}^n/2)$ and $\mathbb{I}$ is the identity block matrix. We apply Schur complement reduction to obtain

$$\begin{bmatrix} \mathbb{E} & \mathbb{F} \\ 0 & -\mathbb{C}\mathbb{E}^{-1}\mathbb{F} \end{bmatrix} \begin{bmatrix} \hat{X}^{n+1} \\ \hat{P}^{n+1/2} \end{bmatrix} = \begin{bmatrix} \mathbb{G}\hat{X}^n \\ -\mathbb{C}\mathbb{E}^{-1}\mathbb{G}\hat{X}^n \end{bmatrix}, \tag{A12}$$

from which we can solve for pressure and subsequently velocity and scalar fields.

920 A26-23

A.2. *Quasi-steady-state approximation*

In the QSSA, the base profiles are assumed to be frozen at a time $\tau_0 > 0$, when they are then perturbed, and the disturbance quantities have the following forms:

$$(u_1, v_1, w_1, Y_1, p_1)$$
$$= [\hat{U}(\eta, \tau_0), \hat{V}(\eta, \tau_0), \hat{W}(\eta, \tau_0), \hat{Y}(\eta, \tau_0), \hat{P}(\eta, \tau_0)] \exp(i(ky + mz - \omega\tau)) + \text{c.c.,}$$
(A13)

where $\omega = \omega_R + i\,\omega_I$, the imaginary part of which indicates temporal perturbation growth rate. This results in a generalized eigenvalue problem with $\tau = \tau_0$ as a parameter (Tan & Homsy 1986), which is then solved with the QZ algorithm (Corbett & Bottaro 2000). The results presented below are for two-dimensional cases ($k = 0$) since $\omega_{I,2D} > \omega_{I,3D}$ for all cases. Figure 16(*a*) displays the imaginary amplification frequency $\omega_I(R, m)$ for uniform viscosity ratio $M = 1$ and $\tau_0 = 10$, where ω_I increases with increasing R. Next, figure 16(*b*) shows $\omega_I(M, m)$ for density ratio $R = 5$ and $\tau_0 = 10$, where the largest ω_I is achieved at the lowest M. Furthermore, figure 16(*c*) shows $\omega_I(\tau_0, m)$ for density ratio $R = 5$ and uniform viscosity $M = 1$ as a function of τ_0. For the largest $\tau_0 = 50$ case considered here, the peak growth rate is the highest among all, but the range of wavenumber m at which $\omega_I > 0$ is the narrowest. The opposite trend is observed at smallest τ_0, where the positive growth rate is seen across a wider range of m, but the peak ω_I is the lowest. Finally, figure 17 displays the typical eigenfunctions obtained from QSSA for $R = 5$, $M = 1$, $\tau_0 = 10$ and $m = 0.05$, which are utilized as initial conditions for the forward integration.

A.3. *Linear IVP – adjoint equations*

The corresponding adjoint equations are

$$D\left(\frac{BZ_0}{\sqrt{\tau^+}}\hat{U}^+\right) + \frac{ikScKZ_0}{2}V^+ + \frac{imScKZ_0}{2}\hat{W}^+ = 0,$$
(A14)

$$\frac{\partial \hat{U}^+}{\partial \tau^+} = D^2\left(\frac{Sc\mu_0 Z_0}{2\tau^+}\hat{U}^+\right) - D\left\{\frac{[(R-1)\mu_0 + 2\beta ScZ_0]Y_0' + 2\eta}{4\tau^+}\hat{U}^+\right\}$$

$$+ \left[i(kV_0 + mW_0\tau^+) - \frac{(k^2+m^2)ScK\mu_0 Z_0}{2} + \frac{(R-1)(\mu_0 Y_0'' + \beta Y_0'^2)}{4\tau^+}\right]\hat{U}^+$$

$$+ D\left(\frac{ikB\mu_0 Z_0}{\sqrt{\tau^+}}\hat{V}^+\right) - \left(\frac{ik\beta BZ_0 Y_0'}{\sqrt{\tau^+}} + \frac{V_0'}{\sqrt{2K\tau^+}}\right)V^+ + D\left(\frac{imB\mu_0 Z_0}{\sqrt{\tau^+}}\hat{W}^+\right)$$

$$- \left(\frac{im\beta BZ_0 Y_0'}{\sqrt{\tau^+}} + \sqrt{\frac{\tau^+}{2K}}W_0'\right)\hat{W}^+ - \frac{Y_0'}{\sqrt{2K\tau^+}}\hat{Y}^+ - \frac{1}{\sqrt{2K\tau^+}}D\hat{P}^+,$$
(A15)

$$\frac{\partial V^+}{\partial \tau^+} = D\left(\frac{ikB\mu_0 Z_0}{\sqrt{\tau^+}}\hat{U}^+\right) + D^2\left(\frac{Sc\mu_0 Z_0}{4\tau^+}V^+\right)$$

$$- D\left\{\frac{[(R-1)\mu_0 + \beta ScZ_0]Y_0' + 2\eta}{4\tau^+}V^+\right\}$$

$$+ \left[i(kV_0 + mW_0\tau^+) - \frac{(2k^2+m^2)ScK\mu_0 Z_0}{2}\right]V^+ - \frac{kmScK\mu_0 Z_0}{2}\hat{W}^+ - ik\hat{P}^+,$$
(A16)

$$\frac{\partial \hat{W}^+}{\partial \tau^+} = D\left(\frac{imB\mu_0 Z_0}{\sqrt{\tau^+}}\hat{U}^+\right) - \frac{kmScK\mu_0 Z_0}{2}V^+ + D^2\left(\frac{Sc\mu_0 Z_0}{4\tau^+}\hat{W}^+\right)$$

$$- D\left\{\frac{[(R-1)\mu_0 + \beta ScZ_0]Y_0' + 2\eta}{4\tau^+}W^+\right\}$$

$$+ \left[i(kV_0 + mW_0\tau^+) - \frac{(k^2 + 2m^2)ScK\mu_0 Z_0}{2}\right]W^+ - im\hat{P}^+, \tag{A17}$$

$$\frac{\partial \hat{Y}^+}{\partial \tau^+} = D\left[\frac{\beta(R-1)BZ_0(\mu_0 Y_0'' + \beta Y_0'^2)}{2\sqrt{(\tau^+)^3}}\hat{U}^+\right] - \left[\frac{i(kV_0' + mW_0'\tau^+)\beta BZ_0}{\sqrt{\tau^+}}\right.$$

$$- \frac{(R-1)^2 B(\mu_0^2 Y_0''' + 4\beta\mu_0 Y_0' Y_0'' + \beta^2 Y_0'^3)}{4Sc\sqrt{(\tau^+)^3}}$$

$$\left. + \frac{\beta(R-1)BZ_0(\mu_0 Y_0''' + 3\beta Y_0' Y_0'')}{2\sqrt{(\tau^+)^3}}\right]\hat{U}^+$$

$$- D\left(\frac{\beta ScZ_0 V_0'}{4\tau^+}V^+\right) + \frac{Sc[\beta Z_0 V_0'' - (R-1)(\mu_0 V_0'' + \beta V_0' Y_0')]}{4\tau^+}V^+$$

$$- D\left(\frac{\beta ScZ_0 W_0'}{4}\hat{W}^+\right)$$

$$+ \left\{\frac{Sc\left[\beta Z_0 W_0'' - (R-1)\left(\mu_0 W_0'' + \beta W_0' Y_0'\right)\right]}{4} - \frac{R^2 - 1}{2R}\right\}\hat{W}^+$$

$$+ D^2\left(\frac{\mu_0 Z_0}{4\tau^+}\hat{Y}^+\right) - D\left\{\frac{[(R-1)\mu_0 + 2\beta Z_0]Y_0' + 2\eta}{4\tau^+}\hat{Y}^+\right\}$$

$$+ \left[i(kV_0 + mW_0\tau^+) - \frac{(k^2 + m^2)K\mu_0 Z_0}{2}\right.$$

$$\left. + \frac{\beta Z_0 Y_0'' - (R-1)(\mu_0 Y_0'' + \beta Y_0'^2)}{4\tau^+}\right]\hat{Y}^+$$

$$+ (R-1)\left\{D^2\left(\frac{\mu_0}{4\tau^+}\hat{P}^+\right) - D\left(\frac{\beta Y_0'}{2\tau^+}\hat{P}^+\right) + \left[\frac{\beta Y_0''}{4\tau^+} - \frac{(k^2 + m^2)K\mu_0}{2}\right]\hat{P}^+\right\}. \tag{A18}$$

The equations above can be expressed in compact form as

$$\frac{\partial \hat{X}^+}{\partial \tau^+} = A^+\hat{X}^+ + B^+\hat{P}^+, \tag{A19a}$$

$$C^+\hat{X}^+ = 0, \tag{A19b}$$

where $\hat{X}^+ = (\hat{U}^+, \hat{V}^+, \hat{W}^+, \hat{Y}^+)$. Taking the derivative of (A19b) with respect to time, we have

$$\frac{\partial C^+}{\partial \tau^+}\hat{X}^+ + C^+\frac{\partial \hat{X}^+}{\partial \tau^+} = 0, \tag{A20}$$

and substituting ([A19a](#)) yields the equation for pressure:

$$\hat{P}^+ = -\left(C^+ B^+\right)^{-1}\left(\frac{\partial C^+}{\partial \tau^+} + C^+ A^+\right)\hat{X}^+. \tag{A21}$$

The pressure can be substituted back into ([A19a](#)) to obtain

$$\frac{\partial \hat{X}^+}{\partial \tau^+} = \left[A^+ - B^+\left(C^+ B^+\right)^{-1}\left(\frac{\partial C^+}{\partial \tau^+} + C^+ A^+\right)\right]\hat{X}^+ \equiv L^+ \hat{X}^+. \tag{A22}$$

Appendix B. Inviscid solution for non-zero velocity difference Δw_0 at $t = t_0 > 0$

We generalize the inviscid formulation in Prathama & Pantano ([2017](#)) to account for a non-zero vertical velocity difference between the two streams in the z direction, Δw_0, at $t = t_0 > 0$, when the infinitesimal perturbation is initially imposed on the base flow. Prior to that, i.e. when $t < t_0$, it is assumed that the base flow is not perturbed. Denoting $\pm$ as the right and left fields with respect to the interface, respectively, the general structure of the equations for perturbation velocities is of the form

$$\frac{\partial \hat{\phi}^{\pm}}{\partial t} \pm imw_0^{\pm}(t)\hat{\phi}^{\pm} = C_0^{\pm}(t), \tag{B1}$$

where

$$w_0^{\pm}(t) = \mp 2a^{\pm}t, \quad a^{\pm} = \frac{R-1}{4R^{\pm}}g, \quad R^+ = R, \quad R^- = 1, \tag{B2a–d}$$

and $C_0^{\pm}(t)$ is the coefficient for the perturbation pressure, whose solution is

$$\hat{p}^{\pm} = C_0^{\pm}(t)e^{\mp \mathcal{K}x}, \tag{B3}$$

where $\mathcal{K}^2 = k^2 + m^2$. The relations between $\hat{\phi}^{\pm}$ and the perturbation velocities are given by

$$\hat{u}^{\pm} = \pm \frac{\mathcal{K}}{\rho^{\pm}}\hat{\phi}^{\pm}e^{\mp \mathcal{K}x}, \quad \hat{v}^{\pm} = -\frac{ik}{\rho^{\pm}}\hat{\phi}^{\pm}e^{\mp \mathcal{K}x}, \quad \hat{w}^{\pm} = -\frac{im}{\rho^{\pm}}\hat{\phi}^{\pm}e^{\mp \mathcal{K}x}. \tag{B4a–c}$$

Solving ([B1](#)) with initial time $t_0 > 0$, we obtain

$$\hat{\phi}^{\pm}(t) = \hat{\phi}_0^{\pm}\exp(\pm ima^{\pm}(t^2 - t_0^2)) + \int_{t_0}^{t} C_0^{\pm}(t')\exp(\pm ima^{\pm}(t^2 - t'^2))\,\mathrm{d}t'. \tag{B5}$$

Following Prathama & Pantano ([2017](#)), the differential equation for the interface amplitude $\hat{\zeta}$ is given by

$$\begin{aligned}
\frac{\partial \hat{\zeta}}{\partial t} \mp 2ima^{\pm}t\hat{\zeta} &= \hat{u}^{\pm}(x=0) \\
&= \pm\frac{\mathcal{K}}{\rho^{\pm}}\left[\hat{\phi}_0^{\pm}\exp(\pm ima^{\pm}(t^2 - t_0^2)) + \int_{t_0}^{t} C_0^{\pm}(t')\exp(\pm ima^{\pm}(t^2 - t'^2))\,\mathrm{d}t'\right],
\end{aligned} \tag{B6}$$

and for zero surface tension, $C_0^+(t) = C_0^-(t)$. Multiplying ([B6](#)) by $\exp(\mp ima^{\pm}t^2)$, taking the derivative with respect to time, cancelling exponential terms on both sides and

920 A26-26

eliminating $C_0^{\pm}$, we obtain

$$\frac{d^2\hat{\zeta}}{dt^2} - \frac{\omega_0^4}{4}t^2\hat{\zeta}(t) = 0, \tag{B7a}$$

with

$$\omega_0^4 = g^2 m^2 \frac{(R-1)^2}{R}. \tag{B7b}$$

Equation (B7a) can be non-dimensionalized by introducing $\tilde{\tau} \equiv \omega_0 t$, giving

$$\frac{d^2\tilde{\zeta}}{d\tilde{\tau}^2} - \frac{\tilde{\tau}^2}{4}\tilde{\zeta} = 0. \tag{B8}$$

The general solution of (B8) can be expressed as

$$\tilde{\zeta}(\tilde{\tau}) = C_1 D_{-1/2}(\tilde{\tau}) + C_2 D_{-1/2}(i\tilde{\tau}), \tag{B9}$$

where $D_j(z)$ denotes the parabolic cylinder function of order j. We require two initial conditions, the first of which is unity interface amplitude $\tilde{\zeta}(\tilde{\tau} = \tilde{\tau}_0) = 1$. The other condition is $\tilde{\zeta}_{\tilde{\tau}}(\tilde{\tau} = \tilde{\tau}_0) = 0$, obtained from setting $t = t_0$ in (B6) and choosing $\hat{\phi}_0^{\pm}$ such that the following condition is satisfied:

$$\mp 2ima^{\pm}t_0 = \pm\frac{\mathcal{K}}{\rho^{\pm}}\hat{\phi}_0^{\pm}. \tag{B10}$$

Finally, the constants are given by

$$C_1 = \frac{\tilde{\tau}_0 D_{-1/2}(i\tilde{\tau}_0) + 2iD_{1/2}(i\tilde{\tau}_0)}{2C_3} \tag{B11}$$

and

$$C_2 = \frac{\tilde{\tau}_0 D_{-1/2}(\tilde{\tau}_0) - 2D_{1/2}(\tilde{\tau}_0)}{2C_3}, \tag{B12}$$

where

$$C_3 = iD_{-1/2}(\tilde{\tau}_0)D_{1/2}(i\tilde{\tau}_0) + D_{-1/2}(i\tilde{\tau}_0)\left[\tilde{\tau}_0 D_{-1/2}(\tilde{\tau}_0) - D_{1/2}(\tilde{\tau}_0)\right]. \tag{B13}$$

REFERENCES

ARRATIA, C., CAULFIELD, C.P. & CHOMAZ, J.-M. 2013 Transient perturbation growth in time-dependent mixing layers. *J. Fluid Mech.* **717**, 90–133.

AURENTZ, J.L. & TREFETHEN, L.N. 2017 Block operators and spectral discretizations. *SIAM Rev.* **59**, 423–446.

BATCHELOR, G.K. 1967 *An Introduction to Fluid Dynamics*. Cambridge University Press.

BEN, Y., DEMEKHIN, E.A. & CHANG, H.-C. 2002 A spectral theory for small-amplitude miscible fingering. *Phys. Fluids* **14**, 999–1010.

BRETHERTON, C.S. 1987 A theory for nonprecipitating moist convection between two parallel plates. Part I: thermodynamics and 'linear' solutions. *J. Atmos. Sci.* **44**, 1809–1827.

BUTLER, K.M. & FARRELL, B.F. 1992 Three-dimensional optimal perturbations in viscous shear flow. *Phys. Fluids* **4**, 1637–1650.

CHANDRASEKHAR, S. 1981 *Hydrodynamic and Hydromagnetic Stability*. Dover.

CORBETT, P. & BOTTARO, A. 2000 Optimal perturbations for boundary layers subject to stream-wise pressure gradient. *Phys. Fluids* **12**, 120–130.

CORBETT, P. & BOTTARO, A. 2001 Optimal linear growth in swept boundary layers. *J. Fluid Mech.* **435**, 1–23.

CRIMINALE, W.O., JACKSON, T.L. & JOSLIN, R.D. 2003 *Theory and Computation of Hydrodynamic Stability*. Cambridge University Press.

DANIEL, D., TILTON, N. & RIAZ, A. 2013 Optimal perturbations of gravitationally unstable, transient boundary layers in porous media. *J. Fluid Mech.* **727**, 456–487.

DOUMENC, F., BOECK, T., GUERRIER, B. & ROSSI, M. 2010 Transient Rayleigh–Bénard–Marangoni convection due to evaporation: a linear non-normal stability analysis. *J. Fluid Mech.* **648**, 521–539.

DRAZIN, P.G. & REID, W.H. 2004 *Hydrodynamic Stability*. Cambridge University Press.

DRISCOLL, T.A., HALE, N. & TREFETHEN, L.N. 2014 *Chebfun Guide*. Pafnuty.

ETRATI, A., ALBA, K. & FRIGAARD, I.A. 2018 Two-layer displacement flow of miscible fluids with viscosity ratio: experiments. *Phys. Fluids* **30**, 052103.

FARRELL, B.F. 1988 Optimal excitation of perturbations in viscous shear flow. *Phys. Fluids* **31**, 2093–2102.

FARRELL, B.F. & MOORE, A.M. 1992 An adjoint method for obtaining the most rapidly growing perturbation to oceanic flows. *J. Phys. Oceanogr.* **22**, 338–349.

FOURES, D.P.G., CAULFIELD, C.P. & SCHMID, P.J. 2014 Optimal mixing in two-dimensional plane Poiseuille flow at finite Péclet number. *J. Fluid Mech.* **748**, 241–277.

GAT, I., MATHEOU, G., CHUNG, D. & DIMOTAKIS, P.E. 2016 Acceleration-driven variable-density turbulent flow. In Proceedings of the VIIIth International Symposium on Stratified Flows (ISSF), San Diego, CA.

GAT, I., MATHEOU, G., CHUNG, D. & DIMOTAKIS, P.E. 2017 Incompressible variable-density turbulence in an external acceleration field. *J. Fluid Mech.* **827**, 506–535.

GUÉGAN, A., SCHMID, P.J. & HUERRE, P. 2006 Optimal energy growth and optimal control in swept Hiemenz flow. *J. Fluid Mech.* **566**, 11–45.

GUSTAVSSON, L.H. 1991 Energy growth of three-dimensional disturbances in plane Poiseuille flow. *J. Fluid Mech.* **224**, 241–260.

HOTA, T.K., PRAMANIK, S. & MISHRA, M. 2015 Nonmodal linear stability analysis of miscible viscous fingering in porous media. *Phys. Rev.* E **92**, 053007.

KAMINSKI, A.K., CAULFIELD, C.P. & TAYLOR, J.R. 2014 Transient growth in strongly stratified shear layers. *J. Fluid Mech.* **758**, R4.

KIM, M.C. & CHOI, C.K. 2011 The stability of miscible displacement in porous media: nonmonotonic viscosity profiles. *Phys. Fluids* **23**, 084105.

KIRSHBAUM, D.J. & STRAUB, D.N. 2019 Linear theory of shallow convection in deep, vertically sheared atmospheres. *Q. J. R. Meteorol. Soc.* **145**, 3129–3147.

LOPEZ-ZAZUETA, A., FONTANE, J. & JOLY, L. 2016 Optimal perturbations in time-dependent variable-density Kelvin–Helmholtz billows. *J. Fluid Mech.* **803**, 466–501.

LU, X. & PANTANO, C. 2020 On mass conservation and solvability of the discretized variable-density zero-Mach Navier–Stokes equations. *J. Comput. Phys* **404**, 109132.

LUCHINI, P. & BOTTARO, A. 2014 Adjoint equations in stability analysis. *Annu. Rev. Fluid Mech.* **46**, 493–517.

MELLADO, J.P. 2017 Cloud-top entrainment in stratocumulus clouds. *Annu. Rev. Fluid Mech.* **49**, 145–169.

OLSON, B.J., LARSSON, J., LELE, S.K. & COOK, A.W. 2011 Nonlinear effects in the combined Rayleigh–Taylor/Kelvin–Helmholtz instability. *Phys. Fluids* **23**, 114107.

PRATHAMA, A.H. & PANTANO, C. 2017 Inviscid linear stability analysis of two vertical columns of different densities in a gravitational acceleration field. *J. Fluid Mech.* **826**, R4.

RAPAKA, S., CHEN, S., PAWAR, R.J., STAUFFER, P.H. & ZHANG, D. 2008 Non-modal growth of perturbations in density-driven convection in porous media. *J. Fluid Mech.* **609**, 285–303.

RAYLEIGH, L. 1883 Investigation of the character of the equilibrium of an incompressible heavy fluid of variable density. *Proc. Lond. Math. Soc.* **14**, 170–177.

REDDY, S.C. & HENNINGSON, D.S. 1993 Energy growth in viscous channel flows. *J. Fluid Mech.* **252**, 209–238.

REDDY, S.C., SCHMID, P.J. & HENNINGSON, D.S. 1993 Pseudospectra of the Orr–Sommerfeld operator. *SIAM J. Appl. Maths* **53**, 15–47.

RIAZ, A., PANKIEWITZ, C. & MEIBURG, E. 2004 Linear stability of radial displacements in porous media: influence of velocity-induced dispersion and concentration-dependent diffusion. *Phys. Fluids* **16**, 3592–3598.

RICHTMYER, R.D. 1960 Taylor instability in shock acceleration of compressible fluids. *Commun. Pure Appl. Maths* **13** (2), 297–319.

SANDOVAL, D.L. 1995 The dynamics of variable-density turbulence. PhD thesis, University of Washington.

SCHMID, P.J. 2007 Nonmodal stability theory. *Annu. Rev. Fluid Mech.* **39**, 129–162.

SCHMID, P.J. & HENNINGSON, D.S. 2001 *Stability and Transition in Shear Flows*. Springer.

SHARP, D.H. 1984 An overview of Rayleigh–Taylor instability. *Physica* D **12**, 3–18.

TAN, C.T. & HOMSY, G.M. 1986 Stability of miscible displacements in porous media: rectilinear flow. *Phys. Fluids* **29**, 3549–3556.

TAYLOR, G. 1950 The instability of liquid surfaces when accelerated in a direction perpendicular to their planes. I. *Proc. R. Soc. Lond.* A **201**, 192–196.

TREFETHEN, L.N., TREFETHEN, A.E., REDDY, S.C. & DRISCOLL, T.A. 1993 Hydrodynamic stability without eigenvalues. *Science* **261**, 578–584.

TRUZZOLILLO, D. & CIPELLETTI, L. 2018 Hydrodynamic instabilities in miscible fluids. *J. Phys.: Condens. Matter* **30**, 033001.